NTNU

Norwegian University of
Science and Technology

Fluid-Structure Interaction in Compressible Viscous Flow

Knut Emil Ringstad

Master of Energy and Environmental Engineering
Submission date: June 2018
Supervisor: Bernhard Müller, EPT

Norwegian University of Science and Technology
Department of Energy and Process Engineering

NTNU
Norwegian University
of Science and Technology

Department of Energy
and Process Engineering

EPT-M-2018-72

MASTER THESIS

for

Student Knut Emil Ringstad

Spring 2018

Fluid-Structure Interaction in Compressible Viscous Flow

Fluid-struktur interaksjon i kompressibel viskøs strømning

Background and objective

Flapping of a flag is a classic example of fluid-structure interaction (FSI) of the wind and the elastic structure of a flag. The prediction of fluid-structure interaction is not only important for flapping flags, but also for flutter of wings and sails as well as understanding the swimming of humans and fish. Another example of fluid-structure interaction is the flapping motion of the soft palate in the human pharynx. During sleep, the soft palate can make contact with the pharynx wall and lead to the obstructive sleep apnea syndrome (OSAS). Also the sound generated by FSI, e.g. FSI of the inhaled air and the soft palate causing snoring, can be of interest. Because of its great importance for public health, OSAS has been investigated in a larger research project entitled Modeling of obstructive sleep apnea by fluid-structure interaction in the upper airways, which is funded by the Research Council of Norway.

The objective of the master thesis is to extend an existing immersed boundary method (IBM) for the 2D compressible Navier-Stokes equations from simulating compressible viscous flow around moving bodies to FSI. Instead of prescribing the motion of a body, the location and velocity of the fluid-solid interface are to be computed by solving a structure equation with the traction supplied by the fluid flow. The FSI approach is to be verified.

The following tasks are to be considered:

1. to get a basic understanding of FSI, its mathematical description and its numerical solution,
2. to extend the existing IBM method for moving bodies to an IBM method for FSI,
3. to verify the FSI method by applying it to a FSI benchmark,
4. to investigate the transfer of energy between fluid and structure.

-- " --

Within 14 days of receiving the written text on the master thesis, the candidate shall submit a research plan for his project to the department.

When the thesis is evaluated, emphasis is put on processing of the results, and that they are presented in tabular and/or graphic form in a clear manner, and that they are analyzed carefully.

The thesis should be formulated as a research report with summary both in English and Norwegian, conclusion, literature references, table of contents etc. During the preparation of the text, the candidate should make an effort to produce a well-structured and easily readable report. In order to ease the evaluation of the thesis, it is important that the cross-references are correct. In the making of the report, strong emphasis should be placed on both a thorough discussion of the results and an orderly presentation.

The candidate is requested to initiate and keep close contact with his/her academic supervisor(s) throughout the working period. The candidate must follow the rules and regulations of NTNU as well as passive directions given by the Department of Energy and Process Engineering.

Risk assessment of the candidate's work shall be carried out according to the department's procedures. The risk assessment must be documented and included as part of the final report. Events related to the candidate's work adversely affecting the health, safety or security, must be documented and included as part of the final report. If the documentation on risk assessment represents a large number of pages, the full version is to be submitted electronically to the supervisor and an excerpt is included in the report.

Pursuant to "Regulations concerning the supplementary provisions to the technology study program/Master of Science" at NTNU §20, the Department reserves the permission to utilize all the results and data for teaching and research purposes as well as in future publications.

The final report is to be submitted digitally in DAIM. An executive summary of the thesis including title, student's name, supervisor's name, year, department name, and NTNU's logo and name, shall be submitted to the department as a separate pdf file. Based on an agreement with the supervisor, the final report and other material and documents may be given to the supervisor in digital format.

☐ Work to be done in lab (Water power lab, Fluids engineering lab, Thermal engineering lab)
☐ Field work

Department of Energy and Process Engineering, 15. January 2018

B. Müller

Bernhard Müller
Academic Supervisor

Abstract

In this master's thesis a ghost-point immersed boundary method for the compressible Navier-Stokes equations using higher order summation by parts operators is described and implemented for two-way coupled fluid-structure interaction (FSI). Two FSI problems are presented: **a)** an elastically mounted circular cylinder in free stream and **b)** an elastic plate attached to a stationary circular cylinder in channel flow.
a) An elastically mounted circular cylinder is modeled as a harmonic oscillator with two degrees of freedom. The harmonic oscillator system is coupled to the flow solver through the drag and lift forces acting on the cylinder and through the imposed boundary conditions at the immersed boundary. The results are compared against those of Yang and Stern [Yang, J., Stern, F., 2012. "A simple and efficient direct forcing immersed boundary framework for fluid-structure interactions". Journal of Computational Physics 231 (15), 5029-5061] at Re=200. The immersed boundary method (IBM) shows a good capability to describe this FSI problem. The harmonic oscillator system is solved numerically by the explicit Euler method and the classical explicit 4-stage Runge-Kutta method. A convergence study of the harmonic oscillator system gave an unexpectedly low order of convergence when external forces were applied. The transfer of energy between the fluid and structure is investigated for the elastically mounted cylinder in free stream.
b) An elastic plate behind a circular cylinder was modeled with the Euler-Bernoulli thin beam model for transverse motion. The plate was implemented with a higher order immersed boundary method to match the FSI benchmark by Turek and Hron [Turek, S., Hron, J., 2007. Proposal for Numerical Benchmarking of Fluid-Structure Interaction Between an Elastic Object and Laminar Incompressible Flow. Vol. 53.]. The systems are coupled through the immersed boundary and the pressure loads on the structure. The results indicate that the IBM describe FSI problems with deformable bodies well compare to the benchmark at Reynolds numbers Re=20 and Re=100. The implementation of the pressure forces on the structure in the FSI coupling was found to cause amplifying errors which made the simulations unstable.

Sammendrag

I denne oppgaven beskrives en ghost-point immersed boundary-metode for de kompressible Navier-Stokes-ligningene for toveiskoblet fluid-strukturinteraksjon (fluid-structure interaction, FSI). Summation by parts-operatorer av høyere orden brukes for estimere de førstoveiskoblettederiverte i ligningsystemene. To problemstillinger med fluid-strukturinteraksjon presenteres: a) En elastisk montert sirkulær sylinder i uforstyrret strømning og b) en elastisk plate festet til en stasjonær, sirkulær sylinder i kanalstrmning.
a) En elastisk montert sirkulær sylinder modelleres som en harmonisk oscillator med to frihetsgrader. Dette systemet kobles med en strømningsløser gjennom drag- og løftkreftene som virker på sylinderen og gjennom grensebetingelsene påsatt ved immersed boundary-grensen. Resultatene blir sammenlignet med resultater fra Yang og Stern [Yang, J., Stern, F., 2012. "A simple and efficient direct forcing immersed boundary framework for fluidstructure interactions". Journal of Computational Physics 231 (15), 5029-5061] med Reynoldstall Re=200. Sammenligningen viser at immersed boundary-metoden kan beskrive fluid-strukturinteraksjoner godt. Det harmoniske oscillator-systemet løses numerisk med den eksplisitte Euler-metoden og den klassiske eksplisitte Runge-Kutta-metoden med fire nivåer. En konvergensstudie av det harmoniske oscillator-systemet ga lavere konvergensorden enn forventet nr eksterne pådrag ble påført. Overføringen av energi mellom fluid og struktur undersøkes for den elastisk monterte sylinderen.
b) En elastisk plate festet til en sirkulær sylinder modelleres med Euler-Bernoullis thin beam-modell for tverrgående bevegelser. Platen ble implementert med en immersed boundary-metode av høyere orden etter Turek- og Hrons fluid-struktur benchmark [Turek, S., Hron, J., 2007. Proposal for Numerical Benchmarking of Fluid-Structure Interaction Between an Elastic Object and Laminar Incompressible Flow. Vol. 53.]. Resultatene indikerer at denne immersed boundary-metoden kan beskrive fluid-strukturinteraksjons problemer med deformerende strukturer godt ved Reynoldstall Re=100 og Re=20. Implementeringen av trykklastene på platen forårsaket selvforsterkende feil som gjorde simuleringene ustabile.

Acknowledgments

I would like to express my most sincere gratitude to my supervisor Bernhard Müller. His support and inspiring guidance have been invaluable for this master's thesis. I would also like to extend my gratitude to Ehsan Khalili for his help with the immersed boundary method (IBM) and for supplying his higher order IBM code for compressible flow around moving bodies.

Table of Contents

List of Tables

List of Figures

List of symbols and abbreviations

Symbols

ρ_f	=	Fluid mass density
μ_f	=	Dynamic fluid viscosity
ν_f	=	Kinematic fluid viscosity
τ	=	Viscous stress tensor
γ	=	Ratio of specific heats
κ	=	Heat conduction coefficient
ϕ	=	Plate displacement
t	=	Physical time
x, y	=	Cartesian coordinates in physical domain
ξ,η	=	Transformed coordinates in computational domain
E	=	Specific total energy
H	=	Total entalpy
p	=	Pressure
Sc	=	Sutherland constant
T	=	Temperature
$\vec{U}$	=	Vector of conservative variables
$\vec{n}$	=	normal vector
St	=	Strouhal number
ρ_s	=	Structure mass density
ν_s	=	Structure Poisson ratio
s	=	Vector of joint points

Abbreviations

GP	=	Ghost point
IP	=	Image point
BI	=	Body intercept
JP	=	Joint point
CFD	=	Computational fluid dynamics
IBM	=	Immersed boundary method
OSAS	=	Obstructive sleep apnea syndrome
SBP	=	Summation by parts
FSI	=	Fluid-Structure Interaction

Chapter 1

Introduction

Computational fluid dynamics (CFD) for biomedical applications has been becoming an increasingly powerful and important tool for the understanding of flows in the human body. Investigations have already been done for many biomedical applications, such as patient-specific models of the nasal flows [31], modeling of the cardiovascular system [13][45], and CFD for the deposition of aerosols in the human lungs [25].

One application of interest is the modeling of airflow through the upper human airways and how this affects obstructive sleep apnea. Obstructive sleep apnea syndrome (OSAS) is a disorder where repetitive closure of the upper airways can cause sleep fragmentation and blood oxygen desaturation. The symptoms of OSAS are daytime sleepiness and heavy snoring [14][27][53]. This has been investigated by Khalili [27] for the research project "Modeling of obstructive sleep apnea by fluid-structure interaction in the upper airways", funded by the Research Council of Norway [34]. To further understand the importance of turbulence in flows in the upper human airways an investigation was done by Aasgrav et al. [1], where different turbulence models were tested. It was found that the effects of turbulence were insignificant for these flows. A better understanding of flows in the upper human airways will allow medical professionals to improve upon and better comprehend the impact of surgical treatment in the nasal cavity. However, the development of CFD tools is hampered by the complexity of the modeling problem. The geometry of the upper human airways is intricate and contains flexible tissue which has to be modeled, cf. Figure 1.1. Furthermore, conventional CFD-software is often of limited use when facing tasks with moving complex geometries, as these require remeshing of the geometry, a computationally heavy and complicated task. This issue is made substantially simpler by the application of non-body-fitted methods. One such method is the immersed boundary method (IBM).

The immersed boundary method was originally developed by Peskin [43] to investigate the flow of blood in the heart. The premise of the method is to define a solid boundary in the fluid domain and indirectly impose the structure boundary conditions at this boundary. Peskin [43] imposes these boundary conditions through a forcing term in the momentum equation. An alternative way was proposed by Fadlun et al. [15], where the boundary con-

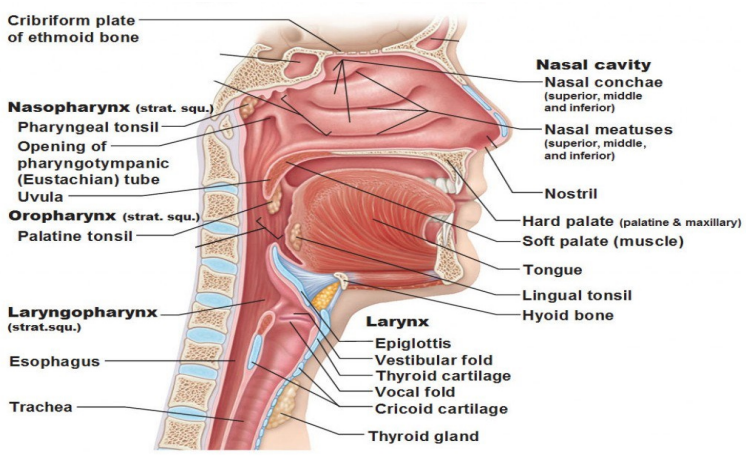

Figure 1.1: Illustration of the human upper airways [41]

ditions are imposed by setting the flow variables inside the immersed boundary such that, on average, the boundary conditions are respected at the immersed boundary. This method came to be called the ghost-cell immersed boundary method (GCIBM). A description of the ghost cell immersed boundary method can be found in Ringstad [46]: ”In CFD, the most conventional and common way to handle boundary conditions, such as a wall, is to make the grid conform to the body and thereby imposing the boundary condition at the grid points fitted to the boundary. This is referred to as a body-fitted grid. The mesh generation of highly complex or moving geometries is a computationally heavy and complicated task for any body-fitted grid. The immersed boundary method avoids this problem by keeping a simple, usually Cartesian grid and treating the boundary conditions at internal boundaries indirectly. This boundary can with much lower computational cost be moved by recalculating where and how to impose the new boundary conditions. In the ghost-point version of the IBM, the indirect imposition of these boundary conditions is done by wisely setting the values of flow variables on the solid side of the boundary. These points are lying inside the solid (see figure 3.1). However, the ghost points are treated by the discretized equations as fluid points, and so they affect the flow variables at the fluid points outside the boundary. Due to their effect on the fluid points without themselves being ”real” fluid points they are referred to as ghost points. Points inside the solid which do not appear in the discretized flow equations are considered solid points. An illustration of this general case is shown in figure (3.1).”

In recent advancements, the immersed boundary method has successfully been implemented alongside the level-set method. The level-set method has been used for an improved description of free surface, two-phase flow [5], and compressible [12] and incompressible flows with stationary or moving bodies [11][48].

Due to its simple implementation for arbitrary geometries, the immersed boundary method is well suited for problems with moving geometries and is as such a good fit for investigating the interactions between deforming structures and surrounding fluid. These types of problems are referred to as fluid-structure interaction (FSI) problems. In fluid-

structure interaction, the equations of fluid motion and the structure model must be solved in parallel and coupled to capture these interactions. The two systems are coupled through the imposed conditions on each other, such as through the kinematic structure boundary conditions in the fluid and the fluid traction on the structure. Fluid-structure interaction has been well utilized for many applications, from aerodynamics [19] to magnetohydrodynamics [17] and biomedical applications [35][7]. The equations and interface conditions in FSI are highly nonlinear and in many cases hard to experimentally verify [22].

The numerical solutions of these problems are often classified by whether the solution of the structure and fluid flow equations are mathematically treated separately or unified, referred to as the *monolithic approach* and the *partitioned approach*, respectively [22]. In the monolithic approach [47][37][23] the fluid and structure equations are solved simultaneously as one system of equations. In the partitioned approach, the fluid and structure equations are solved separately simplifying the implementation and use of codes at the cost of synchronization [22].

The interactions of fluid and structure are, by its nature, multidisciplinary and merge the fields of structure and fluid mechanics. Correct modeling of the structure is critical for a successful combination with a fluid model. Structure dynamics is trying to model the behavior of deformations, stresses, and strains under different assumptions. Many structure models have been applied to FSI problems. Also, the immersed boundary notion has been combined with different structure methodologies. The combination of the finite-element method with the immersed boundary method, as proposed by Zhang et al. [56], shows promise for the simulation of very flexible solids. One of the earliest and simplest models in structure-dynamics is the Euler-Bernoulli thin beam model. This model has already been used for dynamic plate modeling of a simplified soft palate [2][28] and the modeling of plate dynamics behind a cylinder [42]. Results with the Euler-Bernoulli beam model by Garcia [16] compare well with the structure-dynamics results of the benchmark presented by Turek and Hron [52].

To properly describe the FSI, the proper solution of the equations of fluid and structure motion is required. Since the IBM requires high grid resolution, a higher order numerical method is preferable for the solution of these equations. However, such methods are often less stable. A stable way to implement higher order discretizations is using summation by parts (SBP) operators.

The following paragraph is taken from Ringstad [46]. A summation by parts operator is a finite difference method to approximate the first derivative such that the discrete analog of integration by parts is satisfied [18]. That discretization ensures that the energy of a hyperbolic system is bounded by the initial condition. The idea is to get a stable method by devising a discretization scheme such that the energy of the discrete equations behaves similarly as the energy of the continuous hyperbolic partial differential equation. This finite difference method was introduced by Kreiss and Scherer [32][33]. Higher order SBP operators with diagonal discrete norm matrices were devised by Strand [50] with order $2s$ in the interior and order s near the boundaries, $s = 1, 2, 3, 4$. To keep the method stable during time integration a weakly imposed boundary condition was suggested by Carpenter et al. [9]. This is done by a boundary term called the "simultaneous approximation term" (SAT). This term is applying the boundary condition by "dragging" the computed bound-

ary value towards the prescribed boundary value by a differential equation. Later SBP operators of the second space derivative for parabolic problems were devised by Mattsson and Nordström [36].

In this master's thesis, a higher order compressible fluid solver is coupled with different structure models to investigate the fluid-structure interactions of two cases: a) flow over an elastically mounted circular cylinder, and b) flow over an elastic plate attached to a stationary circular cylinder. The cylinder and the attached plate are implemented with the immersed boundary method using three layers of ghost points. The movement of the structures is found from the interactions with the surrounding fluid by a two-way explicit coupling with the arbitrary-Lagrangian-Eulerian (ALE) formulation. The fluid-structure coupling and the rate of energy transfer between the structure and the fluid are investigated. SBP operators are used for the spatial discretization of the fluid equations. The elastically mounted cylinder is modeled by a second-order ODE for harmonic oscillators. The ODE system is solved numerically by the explicit Euler method and the classical explicit 4-stage Runge-Kutta method. Other methods are investigated as well. The elastic plate is modeled by the Euler-Bernoulli thin beam theory and solved by the Newmark method. This thesis is based on the work by Khalili [27] on the immersed boundary method and continues to further investigate fluid-structure interactions using this IBM.

The thesis is structured as follows: In chapter 2, some background theory for compressible flow, harmonic oscillators, and Euler-Bernoulli thin beam theory are presented. In chapter 3 the numerical model is described, and the immersed boundary method and its implementation for an elastic plate are presented. The numerical setup is presented in chapter 4, in which the results of the simulations are shown and discussed. The method is verified against previous results by Yang and Stern [55] for flow over an elastically mounted circular cylinder, cf. section 4.2. The results of FSI simulations of an elastic plate behind a circular cylinder are shown and discussed in section 4.3. The conclusions are given in chapter 5. Lastly, suggestions for further work are presented in chapter 6.

The image shown on the front page is presented in this master's thesis in Figure **??**.

Chapter 2

Governing equations

Sections 2.1-2.2 are restated as presented in the author's project work [46]. The model for the fluid flow solver is described in further detail in Khalili et al. [30].

2.1 Compressible gas dynamics

The 2D compressible Navier-Stokes (NS) equations are considered. These are a system of transport equations: the continuity equation for the density of the fluid (2.1), the momentum equation for the two components of the momentum density (2.2) and the energy equation for the total energy (2.3). This gives four equations for six variables, including the pressure and temperature. The system is closed by the equations of state (2.4-2.5). The compressible Navier-Stokes without external forces can be written with the Einstein summation convention:

$$\frac{\partial \rho}{\partial t} + \frac{\partial}{\partial x_j}\left[\rho u_j\right] = 0, \tag{2.1}$$

$$\frac{\partial}{\partial t}\left(\rho u_i\right) + \frac{\partial}{\partial x_j}\left[\rho u_i u_j + p\delta_{ij} - \tau_{ij}\right] = 0, \quad i = 1, 2, \tag{2.2}$$

$$\frac{\partial}{\partial t}\left(\rho E\right) + \frac{\partial}{\partial x_j}\left[\rho u_j E + u_j p + q_j - u_i \tau_{ij}\right] = 0, \tag{2.3}$$

where ρ, u_1, u_2, p, E are the mass density, x- and y-velocity components, pressure and specific total energy, respectively. δ_{ij} is the Kronecker delta, i.e. =1 if i=j, and =0 else.

The equations of state for perfect gas are used:

$$p = \rho R T, \tag{2.4}$$

$$e = c_v T, \tag{2.5}$$

where $e = E - \frac{1}{2}(u_1^2 + u_2^2)$ is the specific internal energy. R, c_v, T are the gas constant of the fluid, specific heat at constant volume and temperature, respectively. These equations are solved in dimensionless, perturbation form, discussed in section 2.2.

The viscous stress tensor components for Newtonian fluids are defined as:

$$\tau_{ij} = \mu(\frac{\partial u_i}{\partial x_j} + \frac{\partial u_j}{\partial x_i}) - \frac{2\mu}{3}\frac{\partial u_k}{\partial x_k}\delta_{ij}, \tag{2.6}$$

where μ is the viscosity of the fluid. The viscosity is determined by the Sutherland law $\frac{\mu}{\mu_0} = (\frac{T}{T_0})^{1.5}[(1+Sc)/(\frac{T}{T_0}+Sc)]$, where S_c is the dimensionless Sutherland constant, $S_c = \frac{110}{301.75}$, and T_0 is the stagnation temperature. μ_0 is the viscosity at T_0.

The heat flux component q_j is defined as:

$$q_j = -\kappa\frac{\partial T}{\partial x_j}, \tag{2.7}$$

where κ is the thermal conductivity of the fluid.

The pressure can be related to the conservative variables by

$$p = (\gamma - 1)\left(\rho E - \frac{1}{2}\rho(u_1^2 + u_2^2)\right) \tag{2.8}$$

where γ is the ratio of specific heats at constant pressure and volume $\gamma = c_p/c_v$.

2.2 Compressible Navier-Stokes equations

The compressible Navier Stokes equations (2.1-2.3) are expressed in conservative form for the vector of the conserved unknown variables $\vec{U}$:

$$\vec{U} = \begin{pmatrix} \rho \\ \rho u \\ \rho v \\ \rho E \end{pmatrix}. \tag{2.9}$$

The variables are defined in dimensionless, perturbation form. The variables are solved for the perturbation of the variables with respect to the stagnation values, $\vec{U_0} = (\rho_0, 0, 0, (\rho E)_0)^T$, where ρ_0 and $(\rho E)_0$ are the stagnation density and the stagnation total energy density, respectively. This is further described in [29]. The conserved variables are non-dimensionalized by $\rho_0, \rho_0 c_0, \rho_0 c_0, \rho_0 c_0^2$, respectively, where c_0 is the stagnation speed of sound. In this form the compressible Navier Stokes equations can be written as:

$$\vec{U}'_t + \vec{F}^c_x + \vec{G}^c_y = \vec{F}^v_x + \vec{G}^v_y, \tag{2.10}$$

where $\vec{U'} = \begin{pmatrix} \rho' \\ (\rho u)' \\ (\rho v)' \\ (\rho E)' \end{pmatrix}$ with $\rho' = \frac{\rho - \rho_0}{\rho_0}$, $(\rho u)' = \frac{\rho u}{\rho_0 c_0}$, $(\rho v)' = \frac{\rho v}{\rho_0 c_0}$, and $(\rho E)' = \frac{\rho E - (\rho E)_0}{(\rho_0 c_0^2)}$. F and G are the perturbation flux vectors in the *x*- and *y*-directions, respectively. The subscripts indicate differentiation with respect to those variables. The superscript c indicates the convective flux vectors including the pressure terms and v the viscous flux vectors, defined as:

$$\vec{F}^c = \begin{pmatrix} (\rho u)' \\ (\rho u)u' + p' \\ (\rho u)'v' \\ ((\rho H)_0 + \rho H')u' \end{pmatrix} \qquad \vec{G}^c = \begin{pmatrix} (\rho v)' \\ (\rho v)'u' \\ (\rho v)'v' + p' \\ ((\rho H)_0 + \rho H')v' \end{pmatrix} \tag{2.11}$$

$$\vec{F}^v = \begin{pmatrix} 0 \\ \tau_{xx} \\ \tau_{xy} \\ \tau_{xx}u' + \tau_{xy}v' + \kappa T'_x \end{pmatrix} \qquad \vec{G}^v = \begin{pmatrix} 0 \\ \tau_{yx} \\ \tau_{yy} \\ \tau_{yx}u' + \tau_{yy}v' + \kappa T'_y \end{pmatrix} \tag{2.12}$$

where $((\rho H)_0 = (\rho E)_0 + p_0)/\rho_0 c_0^2$ is the nondimensional stagnation total enthalpy per unit volume. $u' = \frac{u}{c_0} = \frac{(\rho u)'}{(1+\rho')}$, $v' = \frac{v}{c_0} = \frac{(\rho v)'}{(1+\rho')}$, $T' = \frac{T-T_0}{T_0}$.

Constant Prandtl numbers $Pr = \frac{\mu c_p}{\kappa}$ were considered, and the ratio of specific heats for air $\gamma = 1.4$ was used. The τ_{ij} terms are here the nondimensional components of the viscous stress tensor of equation (2.6).

Whereas time *t* and the Cartesian coordinates x and y are dimensional variables in section 2.1, they are nondimensional in section 2.2. The reference time and length are $\frac{D}{c_0}$ and D, respectively, where *D* is the diameter of the circular cylinder considered here.

2.3 Coordinate transformation

This section in taken from Ringstad [46]. The fluid flow equations are solved on a 2D Cartesian grid in the transformed coordinates ξ and η. A coordinate transformation $\xi = \xi(x, y)$, $\eta = \eta(x, y)$ is used to improve the resolution near the immersed boundary as seen in figure (2.1). The coordinate transformation is described in [26]. The transformed 2D compressible Navier-Stokes equations are then written as:

$$\hat{\vec{U}}_t + \hat{\vec{F}}_\xi + \hat{\vec{G}}_\eta = 0, \tag{2.13}$$

where $\hat{\vec{U}} = J^{-1}\vec{U}'$, $\hat{\vec{F}} = J^{-1}(\xi_x(\vec{F}^c - \vec{F}^v) + \xi_y(\vec{G}^c - \vec{G}^v))$ and $\hat{\vec{G}} = J^{-1}(\eta_x(\vec{F}^c - \vec{F}^v) + \eta_y(\vec{G}^c - \vec{G}^v))$. The Jacobian determinant of the transformation is $J^{-1} = x_\xi y_\eta - x_\eta y_\xi$ and metric terms are:

$$\begin{aligned} J^{-1}\xi_x &= y_\eta, & J^{-1}\xi_y &= -x_\eta \\ J^{-1}\eta_x &= -y_\xi, & J^{-1}\eta_y &= x_\xi \end{aligned}$$

For simplicity the $\xi-$ and $\eta-$ derivatives will be referred to as the normal x- and y derivatives in this report. This corresponds to the trivial transformation: $\frac{\partial \xi}{\partial x} = 1$, $\frac{\partial \eta}{\partial y} = 1$, $\frac{\partial \xi}{\partial y} = 0$, $\frac{\partial \xi}{\partial x} = 0$.

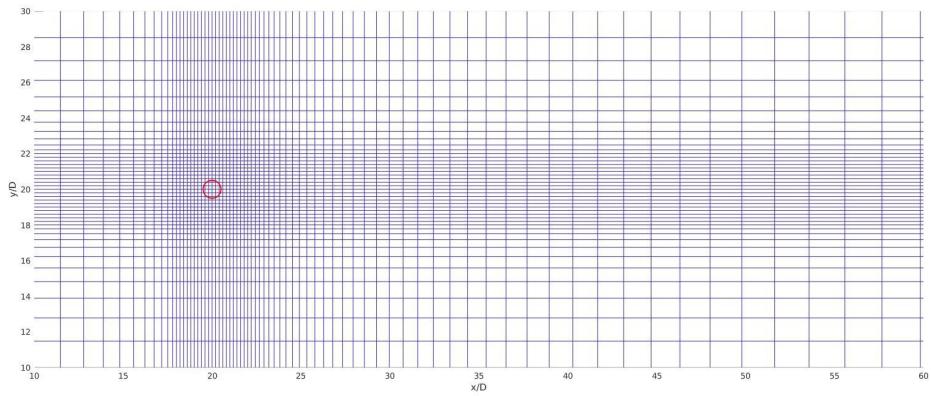

Figure 2.1: Cartesian grid near the circular cylinder for $(x, y)\epsilon$[18D, 22D]x[18D, 22D], and stretched grid away from the cylinder. Every 5th line is plotted

2.4 Harmonic oscillators

The harmonic oscillator is one of the classical engineering problems and finds its applications in many engineering problems where vibrations are of interest. The simplest vibration problems are models for a single point-mass with mass *m* attached to a linear spring with constant stiffness *k*. The position of the point mass with respect to time is described by the function $x(t)$. The spring exerts a force $F_k = -k(x - x_0)$ on the point mass dependent on its displacement from an equilibrium position x_0. This simple system will oscillate around the equilibrium point indefinitely with the frequency $\omega_n = \sqrt{\frac{k}{m}}$. Additional modeling must be added for the loss of energy. The natural process of energy dissipation in such systems is not fully understood [51]. However, these losses will reduce the amplitude of the oscillations. Here this damping is modeled by *viscous damping*, where the damping force is proportional to the velocity through the constant damping *b*, $F_b = -b\frac{dx}{dt}$. For a mass influenced by external forces such as gravity or fluid drag, an external force must be added. Newton's second law of motion yields an ordinary differential equation for the motion of the circular cylinder, $m\frac{d^2x}{dt^2} = F_b + F_k + F_{\text{ext}}$. This law is applied to a 2D cylinder with externally imposed drag and lift forces:

$$m\ddot{x} + b\dot{x} + k(x - x_0) = F_D(t), \tag{2.14}$$

$$m\ddot{y} + b\dot{y} + k(y - y_0) = F_L(t), \tag{2.15}$$

where the lift and drag forces, F_L and F_D, are the external fluid forces decomposed in the x and y-directions. These problems are in literature referred to as a *mass-spring-damper system*, as the system involves only those three components.

The modeling of an elastically mounted circular cylinder in cross flow with FSI is examined to investigate the accuracy of the FSI treatment of the current IBM. The elastic mounting of the cylinder is modeled as a mass-spring-damper system in the x- and y-directions. The cylinder is allowed to move freely in the x- and y directions, restrained by

a spring and damper. The equations of cylinder motion (2.14-2.15) are then written as in [55] for the position variable q, where q correspond to either the x- or y- component of the displacement vector:

$$\ddot{q} + 2\zeta \left(\frac{2\pi}{U^*}\right) \dot{q} + \left(\frac{2\pi}{U^*}\right)^2 q = \frac{2}{\pi m^*} c_{D,L}(t), \tag{2.16}$$

where $\zeta = b/(2\sqrt{km_s})$ is the dimensionless damping, $m^* = \frac{\rho_s}{\rho_f}$ is the dimensionless mass and $U^* = U/(f_N D)$ the dimensionless undisturbed velocity, where $f_N = \frac{1}{2\pi}\sqrt{k/m_s}$ is the natural frequency of the structure and U is the undisturbed fluid velocity away from the cylinder. x and y are nondimensionalized by the cylinder diameter D and t by D/U. $\dot{q} = \frac{dq(t)}{dt}$ and $\ddot{q} = \frac{d^2q(t)}{dt^2}$. The physical quantities k and b are the spring and damping constants, respectively. m_s, ρ_s, and ρ_f are the cylinder mass, the cylinder mass density and the surrounding fluid mass density, respectively. These values were set according to [55] and are presented in section 4.2.1.

The second order ordinary differential equations (ODEs) (2.16) for the displacement components are rewritten as a system of two first order ODEs for the vector of variables $\vec{q} = \begin{pmatrix} x \\ y \end{pmatrix}$.

The system is then rewritten from the form $\ddot{\vec{q}} = f(t, \vec{q}, \dot{\vec{q}})$ into $\dot{\mathbf{Q}} = \mathbf{G}(t, \mathbf{Q})$, where $\mathbf{Q} = \begin{pmatrix} \vec{Q}_1 \\ \vec{Q}_2 \end{pmatrix} = \begin{pmatrix} \dot{\vec{q}} \\ \vec{q} \end{pmatrix}$ and t is the physical time. $\vec{Q}_1 = \begin{pmatrix} \dot{x} \\ \dot{y} \end{pmatrix}$ and $\vec{Q}_2 = \begin{pmatrix} x \\ y \end{pmatrix}$.

The time dependence of f and $\mathbf{G}$ is due to the drag and lift components, $c_D(t)$ and $c_L(t)$, respectively. This gives the system of equations:

$$\frac{d}{dt}\begin{pmatrix} \vec{Q}_1 \\ \vec{Q}_2 \end{pmatrix} = \begin{pmatrix} G_1(t, \vec{Q}_1, \vec{Q}_2) \\ \vec{Q}_1 \end{pmatrix} = \mathbf{G}(t, \mathbf{Q}), \tag{2.17}$$

where the first component of (2.17) corresponds to equation (2.16) solved for the acceleration, i.e., $G_1 = -2\zeta \left(\frac{2\pi}{U^*}\right) \vec{Q}_1 - \left(\frac{2\pi}{U^*}\right)^2 \vec{Q}_2 + \frac{2}{\pi m^*} \begin{pmatrix} c_D(t) \\ c_L(t) \end{pmatrix}$.

2.5 Elastic plate

The Euler-Bernoulli thin beam theory will be applied for the modeling of a deformable elastic plate. A beam is defined by its geometry having one dimension longer than the other two [4]. This is the axial dimension of the beam. The Euler-Bernoulli model attempts to relate the transverse motion to the applied load normal to the axial direction. The axial forces and transverse shear forces are neglected [4]. The Euler-Bernoulli theory also requires constant density and stiffness along the beam length. Under these restrictions, the Euler-Bernoulli theory can model the transverse motion of the plate to a sufficient degree for FSI-application [27]. The displacements perpendicular to the neutral axis can then be described by a function along the plate length $\phi(t, x)$. The plate is influenced by the internal shear forces and external forces. The external forces are introduced through the pressure difference, δp, on either side of the plate. The shear forces are applied through

the variation of the bending moment, *M*, across the beam axis. The bending moment is related to the curvature of the plate through: $M(x,t) \approx -EI\frac{\partial^2\phi}{\partial x^2}$, where *E* is the Young modulus and *I* is the moment of inertia. For further details see [4][27]. This yields the equation for the vertical displacement of the centerline of the beam expressed as:

$$\rho_s h\frac{\partial^2\phi}{\partial t^2} + d\frac{\partial\phi}{\partial t} + B\frac{\partial^4\phi}{\partial x^4} = -\delta p, \tag{2.18}$$

where ρ_s is the structure density and *h* the plate thickness. Damping can also be applied to the equations through the damping term $d\frac{\partial\phi}{\partial t}$, where *d* is the structural damping. This was not applied in these simulations. The flexural rigidity *B* is defined by $B = EI = \frac{Eh^3}{12(1-\nu^2)}$, where ν is the Poissons ratio.

The length and time were non-dimensionalized as for the fluid solver with respect to the reference length *D* and the reference time scale $\frac{D}{c_0}$. The mass $m = \rho_s h$, damping *d* and stiffness *B* were nondimensionalized using the fluid stagnation density ρ_0, speed of sound c_0, cylinder diameter D, and reference pressure $\rho_0 c_0^2$. These non-dimensional quantities are presented in table 2.1. The gravitational load $-\rho_s gh$ was not imposed on the system

Table 2.1: Dimensionless variables of equation 2.18. The apostrophe indicating the dimensionless quantity.

B'	$\frac{B}{\rho_0 c_0^2 D^3}$
d'	$\frac{d}{\rho_0 c_0}$
m'	$\frac{\rho_s h}{\rho_0 D}$

in these simulations. However, as it was used in [16] to evaluate the accuracy of the model it is included here for completeness. The plate is attached to the cylinder at the leading edge of the plate, $x = 0$, by clamping and allowed to freely move in the y-direction at the trailing edge, $x = L$, where L is the length of the plate. These boundary conditions read in continuous form [28]:

$$\phi(t,0) = 0,, \tag{2.19}$$

$$\frac{\partial\phi(t,0)}{\partial x} = 0, \tag{2.20}$$

The boundary conditions at the free end can, under the assumption of zero bending moment and zero shear force, be written:

$$\frac{\partial^2\phi(t,L)}{\partial x^2} = 0, \tag{2.21}$$

$$\frac{\partial^3\phi(t,L)}{\partial x^3} = 0, \tag{2.22}$$

Chapter 3

Discretization

The immersed boundary method is described in section 3.1. The discretization of the flow equations, the mass-spring-damper system and the elastic plate is described in sections 3.2.1, 3.2.2 and 3.2.3, respectively. The fluid-structure coupling is outlined in section 3.2.4. Special attention is given to the implementation of the plate model which is described in detail in section 3.3.

3.1 Ghost point immersed boundary method

The immersed boundary method is a method to impose solids in a discretized fluid domain. It imitates a boundary between the solid and the fluid by imposing boundary conditions that correspond those of a solid wall at this boundary. The boundary between solid and fluid is referred to as the immersed boundary as the solids are ”immersed” into the fluid domain. In the IBM by Khalili et al. [29], the solids are immersed into the fluid domain by imposing boundary conditions with the ghost point methodology. In this methodology, the fluid domain is discretized with a Cartesian grid. The solid is introduced by defining the immersed boundary. Each point inside the immersed boundary is identified as a solid point and points outside the immersed boundary are labeled as fluid points. To impose the boundary conditions at the immersed boundary the points inside the solid are used. The solid points near the boundary that appear in the discretization of the fluid flow equations are called ghost points, cf. Figure 3.1. Khalili et al. [29] uses three layers of ghost points to impose the solid boundary conditions. This is necessary as the higher order flow solver uses three neighboring points in its discretization.

The flow variables at these ghost points are chosen such that, when averaged over the flow variables adjacent to the boundary, the boundary condition is respected at the immersed boundary. A line normal to the immersed boundary is extended from the ghost point. The point of intersection between the immersed boundary and the normal line is called the boundary intersection point (BI). The image point (IP) is found by reflecting the ghost point about the boundary intersection point along the normal line, cf. Figure 3.1. The value of the flow variables at the image point is found by bi-linear interpolation from

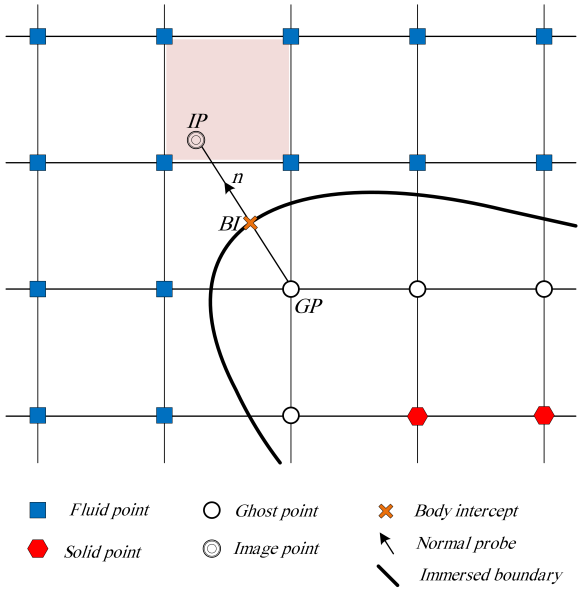

Figure 3.1: Illustration of the ghost-, image- and boundary intersect-points [29]

the nearby fluid points, this is discussed in more detail in [27].

The imposition of the boundary conditions is described in [46]: "To implement the physical boundary conditions at the boundary of the body the ghost points are given values such that the correct condition is applied at the immersed boundary. For a generic variable ϕ a Dirichlet condition would be imposed by setting the ghost point value ϕ_{gp} such that the average of the ghost point value and the value at its corresponding image point (ip) imposes the condition $\phi_{bi} = \phi_{boundary}$, where bi is the boundary intersection point, that is to say, equation (3.1) holds. As mentioned above, the present IBM solver uses a higher order flow solver, which requires three layers of ghost points. An illustration is given in figure (3.2) of how multiple layers the different ghost points are treated.

$$\frac{\phi_{gp} + \phi_{ip}}{2} = \phi_{bi} \tag{3.1}$$

A Neumann condition, $\frac{\partial \phi}{\partial n} = \beta$, can be similarly imposed by setting the ghost point value such that the change of ϕ across the boundary is the given condition β. Thus, the ghost point value ϕ_{gp} should be set such that difference approximation of $\frac{\partial \phi}{\partial n}$ using the difference between the ghost point value and the image point value over the distance between them imposes the boundary condition. This is described by":

$$\frac{\phi_{ip} - \phi_{gp}}{\Delta l} = \beta. \tag{3.2}$$

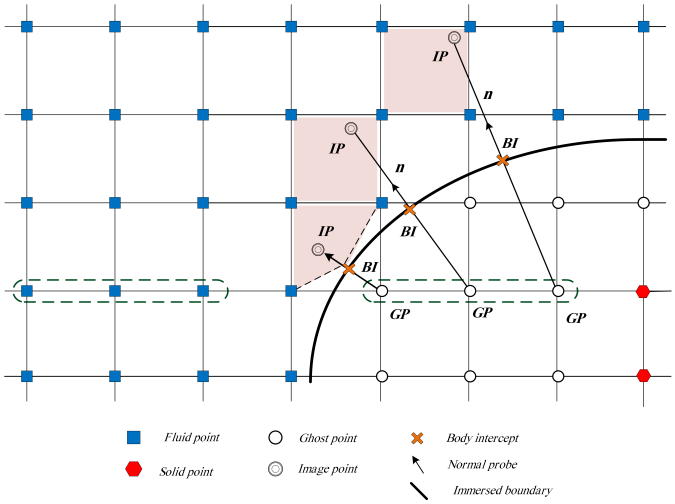

Figure 3.2: Illustration of the ghost-, image- and boundary intersect-points, [26]

3.1.1 Ghost point imposed boundary conditions

The boundary conditions imposed at the structure boundaries used in this thesis are presented here as in [46]: "The physical boundary conditions imposed at solid boundaries are discussed here. For compressible flow, four boundary conditions are needed to close the system. The boundary conditions used in the work by [27] are the no slip-condition for the velocity, the adiabatic wall Neumann condition for the temperature and the boundary layer approximation Neumann condition for the pressure.

$$\vec{u} = \vec{U}_{wall}, \tag{3.3}$$

$$\frac{\partial T}{\partial n} = 0, \tag{3.4}$$

$$\frac{\partial p}{\partial n} = 0, \tag{3.5}$$

where $\vec{U}_{wall}$ is the prescribed velocity of the wall and n denotes the wall normal direction.

By the perfect gas law; $\rho = \frac{RT}{P}$ (2.4), the boundary condition for the density can be found, closing the system and enforcing the adiabatic wall condition eqn. (3.4) by":

$$\frac{d\rho}{dn} = \frac{d(\frac{RT}{p})}{dn} = 0. \tag{3.6}$$

In this thesis, the immersed boundary method is used to impose a circular cylinder and a deformable plate. In the present work, the boundary conditions above are imposed at the immersed boundary. The center of the circular cylinder is used to define the immersed boundary a radius $\frac{D}{2}$, where D is the cylinder diameter, away from the cylinder center point. The image point is then found further along in the radial direction, with respect to the cylinder center, from the ghost point. The cylinder velocities are imposed through the

velocity boundary conditions at the immersed boundary. The cylinder velocity is found by FSI for the case of an elastically mounted circular cylinder. In the case of an elastic plate attached to a circular cylinder, the cylinder was stationary. The implementation of the elastic plate is described in section 3.3.

The immersed boundary is well suited for complex and deforming solid geometries, however, it has its limitations. A high number of grid points near solid surfaces is required to accurately describe the boundary layer near solid walls. To have a very fine grid in the entire discretized domain is if often computationally unrealistic and not necessary to capture the flow phenomena of interest. In a Cartesian grid system, grid refinements are needed in all directions. However, for body-fitted grids, grid refinement only to capture a boundary layer is easily implemented. A grid transformation, such as described in section 2.3, or adaptive mesh refinement [24] is then often needed to get the desired fine grid. If the geometry of the boundary has a sharp turn, such as near the trailing edge of a wing profile, the body may contain fewer ghost points than is needed for higher order discretization. The method would then require special treatment. Other issues appear when the immersed boundary creates small sub-domains that do not hold enough points for a higher order discretization, such an issue is further discussed in section 3.3.

3.2 Numerical method

The fluid-structure interaction problems investigated in this thesis are solved with a partitioned approach, as the fluid and structure systems are solved as two separate systems coupled at the immersed boundary.

3.2.1 Flow solver

This section is taken from the author's project work [46]. The present immersed boundary method uses the standard central 6th order accurate finite difference stencil for the discretization of the first derivatives in space in the interior, i.e. the $\vec{F}^c_\xi, \vec{G}^c_\eta, \vec{F}^v_\xi, \vec{G}^v_\eta$ -terms in equation (2.13). The viscous flux vector terms, $\vec{F}^v, \vec{G}^v$, in equation (2.12) need additional discretizations for their internal derivative terms, i.e., τ_{ij} and $(\kappa T)_\xi, (\kappa T)_\eta$. This is done by applying the first derivative approximation again. Near the boundaries of the domain and near the immersed boundary a sixth order SBP operator with 3rd order, finite difference approximation near the boundaries is applied. The method as a whole gives a global 4th order of accuracy in space [18][50]. The spatial discretization is based on a summation by parts operator. By the energy method that operator will guarantee stability and will keep the energy of the system bounded by the initial conditions if proper boundary conditions are applied. The in- and outflow boundary conditions are applied by injection of the Navier-Stokes characteristic boundary condition [29][44].

For the time discretization of the fluid solver, the classical explicit 4-stage Runge-Kutta method is used giving a 4th order accurate solution in time.

3.2.2 Numerical solution of mass-spring-damper system

This ODE-system (2.17) was solved numerically with the Euler, Heun, Størmer-Verlet and Runge-Kutta 4-stage methods discussed below.

Euler's method

The first method used is the explicit Euler method. The ODE-system (2.17) is evaluated at the old time step, in semi-discrete form written as:

$$\frac{d\mathbf{Q}^n}{dt} = \mathbf{G}(t^n, \mathbf{Q}^n). \tag{3.7}$$

The time derivative is approximated by the first order forward difference approximation. By this, the solution at the new time step can be evaluated by:

$$\mathbf{Q}^{n+1} = \mathbf{Q}^n + \Delta t \mathbf{G}(t^n, \mathbf{Q}^n) \tag{3.8}$$

This method was also used for the solution of the mass-spring-damper system when coupled with FSI, see section 4.2.1.

Heun's method

The second method investigated was Heun's method. Heun's method corresponds to a two-stage Runge-Kutta method. It calculates in the first stage $\mathbf{k} = \mathbf{G}(t^n, \mathbf{Q}^n)$. From the first stage the system is moved forward to time level $n + 1$ by:

$$\mathbf{Q}^{n+1} = \mathbf{Q}^n + \frac{\Delta t}{2} \left(\mathbf{k} + \mathbf{G}(t^n + \Delta t, \mathbf{Q}^n + \mathbf{k}\Delta t) \right). \tag{3.9}$$

Størmer- Verlet method

The third investigated method is the Størmer- Verlet method. Numerical methods have been developed for the preservation of different invariants in the system. Methods such as the Størmer-Verlet method are designed to be *symplectic* for a smooth Hamiltonian system, that is that the method preserves the area in the solution space. The Hamiltonian corresponds to the *total energy* of the system [20]. Neglecting the damping, the Hamiltonian *H* can be written as a function of the position *q* and the momentum, $p = m\dot{q}$:

$$H(p, q) = \frac{1}{2m}(p^2 + kmq^2), \tag{3.10}$$

such that $p_t = -H_q$ and $q_t = H_p$, where the subscript implies differentiation by that variable. With damping this system cannot be considered Hamiltonian, as the *total energy* decays with time.

The Størmer- Verlet method [20] treats the position system and the velocity system differently, here only an intermediate value for the velocity is computed. The method reads:

$$Q_1^{n+1/2} = Q_1^n + \frac{\Delta t}{2} G_1(Q_2^n, Q_1^n) \tag{3.11}$$

$$Q_2^{n+1} = Q_2^n + \Delta t Q_1^{n+1/2} \tag{3.12}$$

$$Q_1^{n+1} = Q_1^{n+1/2} + \frac{\Delta t}{2} G_1(Q_2^{n+1}, Q_1^{n+1/2}). \tag{3.13}$$

This method did not take into consideration damping in its original form. In this system Q_1^{n+1} should be evaluated using G_1 evaluated at time level $n + 1$. However as G_1^{n+1} is dependent on Q_1^{n+1} through the damping term, the system would be implicit. This value is not yet evaluated. In the simulations, the function G_1 was evaluated with the with the intermediate velocity $Q_1^{n+1/2}$ to keep the explicit form. This is thought to have reduced the order of the method, cf. section 4.2.4.

4-stage Runge Kutta method

The classical explicit 4-stage Runge-Kutta method was also investigated. The solution of the system is done by regarding the intermediate values of the Runge Kutta stages $\mathbf{k}_m, \{m = 1, 2, 3, 4\}$, as estimates of the acceleration and velocity $\dot{\mathbf{Q}}(t^n + \Delta t_m)$ at the intermediate times of the 4-stage Runge Kutta method. Here the time step vector of the

4-stage Runge-Kutta method is $(\Delta t_1, ..., \Delta t_4)^T = \left(0, \frac{\Delta t}{2}, \frac{\Delta t}{2}, \Delta t\right)^T$. The stages are then evaluated by:

$$\mathbf{k}_m = \mathbf{G}(t^n + \Delta t_m, \mathbf{Q}^n + \mathbf{k}_{m-1}\Delta t_m), \{m = 1, 2, 3, 4\}. \tag{3.14}$$

Here $\mathbf{k}_0$ corresponds to the acceleration and velocity at time t^n, i,e., $\dot{\mathbf{Q}}^n$. From the Runge-Kutta stages, the solution at the new time level is calculated as:

$$\mathbf{Q}^{n+1} = \mathbf{Q}^n + \Delta t \left(\frac{1}{6}\mathbf{k}_1 + \frac{1}{3}\mathbf{k}_2 + \frac{1}{3}\mathbf{k}_3 + \frac{1}{6}\mathbf{k}_4\right). \tag{3.15}$$

These evaluations require that the time dependencies of $\mathbf{G}(t^n + \Delta t_m, \mathbf{Q}^n + \mathbf{k}_{m-1}\Delta t_m)$ are evaluated, and thereby the values of $c_D(t^n + \Delta t_m)$ and $c_L(t^n + \Delta t_m)$ have to be calculated. In the uncoupled system, this is done by computing the analytical function values $c_D(t^n + \Delta t_m)$ and $c_L(t^n + \Delta t_m)$. The system was also solved coupled to the flow solver. To do this the lift and drag coefficients had to be recalculated in each intermediate stage. This was done by moving the immersed boundary of the cylinder according to the estimates of acceleration and velocity at each intermediate stage, *m*. The corresponding flow variables are evaluated as $U'^{(m)} = U'^n + \mathbf{k}_{m-1}\Delta t_m$, where $\mathbf{k}_m = \mathbf{R}(t^n + \Delta t_m, U'^{(m)})$ with $\mathbf{R}$ the residual of the discretized compressible Navier-Stokes equations (2.10). From this, the drag and lift coefficients were recalculated and imposed at the corresponding time stage levels as $c_D(t^n + \Delta t_m)$ and $c_L(t^n + \Delta t_m)$, respectively. This is presented as a pseudo-code in section 3.2.4 b).

The results of this method when coupled with FSI are presented in section 4.2.1.

3.2.3 Numerical solution of plate model

The Euler-Bernoulli beam theory was used to model the plate motion. Equation (2.18) was numerically solved with the second order accurate implicit Newmark method [39], implemented for an infinitely thin plate in Khalili et al. [28]. The Newmark method solves for the displacement and velocity by using the velocity and acceleration evaluated at the old and new time steps weighted by the factors γ and β. The integration from time level n to $n + 1$ is calculated by[39]:

$$\dot{\phi}^{n+1} = \dot{\phi}^n + \left((1-\gamma)\ddot{\phi}^n + \gamma\ddot{\phi}^{n+1}\right)\Delta t, \tag{3.16}$$

$$\phi^{n+1} = \phi^n + \dot{\phi}^n\Delta t + \left[(\frac{1}{2} - \beta)\ddot{\phi}^n + \beta\ddot{\phi}^{n+1}\right]\Delta t^2. \tag{3.17}$$

The coefficient values used were $\gamma = \frac{1}{2}$ and $\beta = \frac{1}{4}$, which yield unconditional stability and the best accuracy of the Newmark methods [28].

The attached edge is clamped corresponding to the boundary conditions (2.19) and (2.20). These boundary conditions read in discrete form:

$$\phi_1 = 0, \tag{3.18}$$

$$\phi_2 = \phi_2. \tag{3.19}$$

The boundary condition at the free end (2.21) and (2.22), are written in discrete form:

$$\phi_{N-1} = 2\phi_{N-2} - \phi_{N-3}, \tag{3.20}$$

$$\phi_N = 3\phi_{N-2} - 2\phi_{N-3}. \tag{3.21}$$

3.2.4 Fluid-structure coupling

Two methods were used to solve the mass-spring-damper ODE with FSI, the classical explicit Runge-Kutta 4-stage method, and the explicit Euler method. The explicit Euler method for the mass-spring-damper system was implemented in the fluid solver to integrate the movement of the cylinder from time level n to time level $n+1$. First, the structure equations are solved based on the fluid coupling, i.e., the forces drag and lift forces on the cylinder at time level n, to find the new velocities and positions at time level $n+1$. The cylinder is then moved to the new position at time level $n+1$. The structure velocities and displacements at time level $n+1$ are imposed at the immersed boundary when the fluid flow system is integrated to find $\mathbf{U}'^{n+1}$ from $\mathbf{U}'^{n}$. At all intermediate time levels of the Runge-Kutta flow solver, the structure state at time level $n+1$ is then imposed instead of estimates of the structure position and velocities at their corresponding intermediate time stages. This introduces a time integration error. A pseudo-code of the algorithm from time level n to $n+1$ with the explicit Euler method structure solver for the calculation of moving immersed boundaries is included below for clarity. The same way of moving the elastic plate was used with the Newmark method.
a) Pseudo code for explicit Euler/Newmark algorithm

1: Solve the mass-spring-damper system (2.17) or the Euler-Bernoulli thin beam equation (2.18) based on forces or pressure loads, respectively, at time level n.
Move boundary to time level $n+1$.
Set the classical Runge- Kutta stage level $m = 1$.

2: Determine the ghost points values u_{gp}, v_{gp}, ρ_{gp} and p_{gp} using the boundary conditions (3.3-3.6) at three layers of ghost points based on solution $U'^{(m)}$.

3: Compute approximations of the viscous fluxes F^v and G^v, eqn. (2.12), at all fluid and ghost points using the sixth order SBP operator on each line in ξ- and η- directions, respectively.

4: Compute the residual $R(U'^{(m)})$ based on the approximations of the derivatives $\hat{F}_\xi$ and $\hat{G}_\eta$ at all fluid points determined by using the sixth order SBP operator on each line in x- and y- directions, respectively, but the standard sixth order difference operator near the immersed boundary.

5: Determine $U'^{(m+1)}$ using the classical Runge-Kutta method.

6: Apply the Navier Stokes characteristic boundary condition at inlet and outlet and apply the necessary boundary conditions at the bottom and top boundaries to determine $U'^{(m+1)}$ at those boundaries.

7: Set $m := m + 1$.

8: **if** $m < 5$ **then**

9: **goto** 2

10: **else**

11: Compute U^{n+1} at all fluid points.

12: Apply sixth order filter operators in x and y directions at all fluid points [27].

13: **end if**

The classical explicit Runge-Kutta method was implemented for the structure solver for the mass-spring-damper system. The Runge-Kutta structure solver was solved in parallel with the Runge-Kutta flow solver in an alternating manner. At each stage the intermediate flow variables, $U'^{(m+1)}$, are used to estimate the forces exerted on the structure as discussed in section 3.2.2. From these forces, the new position and velocity at the structure intermediate time levels are evaluated. Those intermediate evaluations of the structure velocities are used to move the cylinder. These velocities were also imposed as the velocity boundary conditions at the cylinder surface at their corresponding intermediate Runge-Kutta flow stage. This was done to ensure that the Runge-Kutta flow solver was synchronous with the Runge-Kutta structure solver which would reduce the numerical time integration error. The pseudo code for the synchronous classical explcit Runge-Kutta flow and structure solver is shown below:

b) Pseudo code for classical explicit Runge-Kutta 4-stage algorithm

Set the classical Runge- Kutta stage level $m := 1$.

1: **if** $m < 4$ **then**

2: Solve the mass-spring-damper system (2.17) based on forces at time level $m-1$ for the intermediate accelerations and velocities $\mathbf{k}_{m-1}$. $m = 0$ corresponds to time level n.
Move boundary according to intermediate time level m based on $\mathbf{k}_{m-1}$.

3: **else**
Find the position and velocity at time level $n+1$ from equation (3.15).
Move boundary to time level n + 1.

4: **end if**

5: Determine the ghost points values u_{gp}, v_{gp}, ρ_{gp} and p_{gp} using the boundary conditions (3.3-3.6) at three layers of ghost points based on solution $U'^{(m)}$. The imposed no-slip velocity corresponds to the intermediate structure velocity at stage m.

6: Compute approximations of the viscous fluxes F^v and G^v, eqn. (2.12), at all fluid and ghost points using the sixth order SBP operator on each line in $\xi-$ and $\eta-$ directions, respectively.

7: Compute the residual $R(U'^{(m)})$ based on the approximations of the derivatives $\hat{F}_\xi$ and $\hat{G}_\eta$ at all fluid points determined by using the sixth order SBP operator on each line in $\xi-$ and $\eta-$ directions, respectively, but the standard sixth order difference operator near the immersed boundary.

8: Determine $U'^{(m+1)}$ using the classical RungeKutta method.

9: Apply the Navier Stokes characteristic boundary condition at inlet and outlet and apply the necessary boundary conditions at the bottom and top boundaries to determine $U'^{(m+1)}$ at those boundaries.

10: Set $m := m + 1$.

11: **if** $m < 5$ **then**

12: **goto** 4*

13: **else**

14: Compute U^{n+1} at all fluid points.

15: Apply sixth order filter operators in x- and y directions at all fluid points [27].

16: **end if**

Here m corresponds to the stage number of the classical explicit Runge-Kutta method, n corresponds to the time level. The mentioned filter in step 12 for a) and 15 for b) is further explained in [29].

The equations (2.18) or (2.14-2.15) are coupled to the fluid solver through the pressure load term, $-\delta p$ and $c_{D,L}$ respectively. The pressure difference driving the plate model $-\delta p$ is calculated as the difference between the top and bottom of the plate at the immersed boundary in the fluid, this is further discussed in section 3.3. The lift and drag coefficients of the elastically mounted cylinder are at each time level, or at calculated each intermediate stage when solved simultaneously, by integration of pressure and friction forces over the cylinder surface.

The coupling from the structure system to the fluid flow system is done through the boundary conditions imposed at the immersed boundary. The conditions of equation (3.3 - 3.6) are therefore indirectly imposed at the ghost points near the immersed boundary.

3.3 Implementation of a deformable plate with immersed boundary method

The elastic plate trailing a circular cylinder described by Turek and Hron [52] is to be implemented in this solver by the immersed boundary method. A summary of the geometry used in this report is given in Table 4.1 and shown in Figure 4.1.

The plate model used, i.e. the Euler-Bernoulli thin beam equations (2.18), is described by the displacement $\phi(x)$ about the center line of the plate at *y*=2D. This model is based on a thin plate assumption as the plate thickness goes to zero. Instead of considering this infinitely thin plate an artificial thickness, *h*, was added to the center line. This has the benefit of being able to include ghost points without special treatment.

To describe the flexible plate, the displaced centerline is parameterized by a vector of connecting joints which will be referred to as joint points (jp), $\mathbf{s}(t) = \left(\mathbf{s}^{(1)}(t), ..., \mathbf{s}^{(m)}(t)\right)^T$. Here m is the number of joint points in the plate vector and the components of $\mathbf{s}^{(i)}$ are the x- and displaced y-coordinates at joint i, $\mathbf{s}^{(i)} = \left(x^{(i)}, y^{(i)} - y_0\right)$, such that **s** describes the displaced center line of the plate. This is illustrated in Figure 3.3.

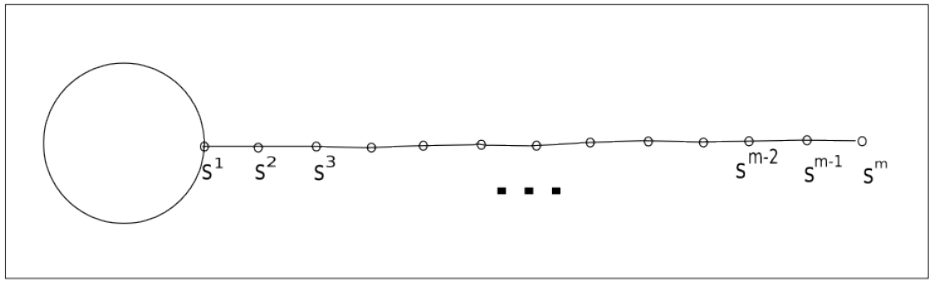

Figure 3.3: Illustration of the joint point vector $\mathbf{s}(t)$ of an elastic plate attached to a circular cylinder.

From this displaced centerline the immersed boundary defining the boundary between fluid and structure can be identified by adding half the plate thickness *h* in the normal direction of the plate. With this immersed boundary the ghost points are identified. This is done by regarding all grid points within a distance $\frac{h}{2}$ from the centerline and a radius $\frac{h}{2}$ from the end joint $s^{(m)}$ as inside the structure and therefore a solid point and all points outside as fluid points. All solid points that have at least one fluid point among its three neighboring points in the positive or negative x- or y-directions are then identified as ghost points. To each ghost point, a projection point *(pr)* is assigned corresponding to the point projected from the ghost point onto the displaced center line **s** along the normal of the center line **s**. This is implemented by this short algorithm:
- For each ghost point take the closest joint point $\mathbf{s}^{(l)}$ to the ghost point, where *l* is the number in the joint point vector corresponding to this point.
- Make two line segments, one to the right of joint point *l* between the points $\mathbf{s}^{(l)}$ and $\mathbf{s}^{(l+1)}$, and one to the left, between points $\mathbf{s}^{(l-1)}$ and $\mathbf{s}^{(l)}$.
- Take the normal from these two line segments and project the ghost point onto both line

segments. Denote the points from the right and left segments by R and L, respectively. The closest point of L and R to the ghost point is selected to be the correct projection point of the ghost point, cf. Figure 3.4.
-The normal of the line segment with the projection point, $\vec{n}$, is then used to find the image point, which is found by reflection about the immersed boundary. The immersed boundary is found at a distance $\frac{h}{2}$ along the normal line $\vec{n}$, cf. Figure 3.5 (upper).

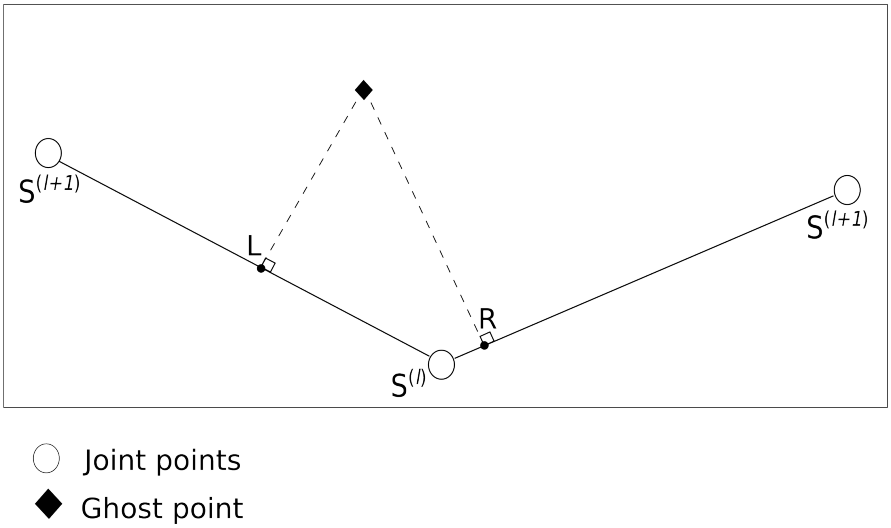

Figure 3.4: Illustration of how the projection points are found

A special treatment is needed near the connection between the plate and the cylinder. Ghost points inside the cylinder find their image point by reflection about the cylinder circumferential boundary. However, near the plate attachment, there are ghost points that find their image points inside the solid plate when reflected about the cylinder circumference. These ghost points are instead given image points reflected about the attachment point, i.e., the point where the plate immersed boundary would meet the cylinder immersed boundary, cf. Figure 3.5(lower). The distance between the ghost point and the attachment point was used to find the image point. Taking this distance from the ghost point along the line that connects the ghost point and the attachment point the image point was identified, cf. Figure 3.5(lower). This corresponds to reflection about an artificial boundary. In Figure 3.5(lower) original image point is the image point found by reflection about the cylinder circumference, and artificial image point is the new artificially moved image point.

The plate end was rounded which was not done in [52]. This was done here to avoid problems surrounding the corners at the plate end. Near these corners, the plate could produce a situation where there were not enough ghost points to properly impose the immersed boundary conditions were available. The rounding of the trailing edge of the plate expected to change some of the near plate-end dynamics. But is not expected to massively influence the plate oscillations over the whole plate as the length is much larger than the

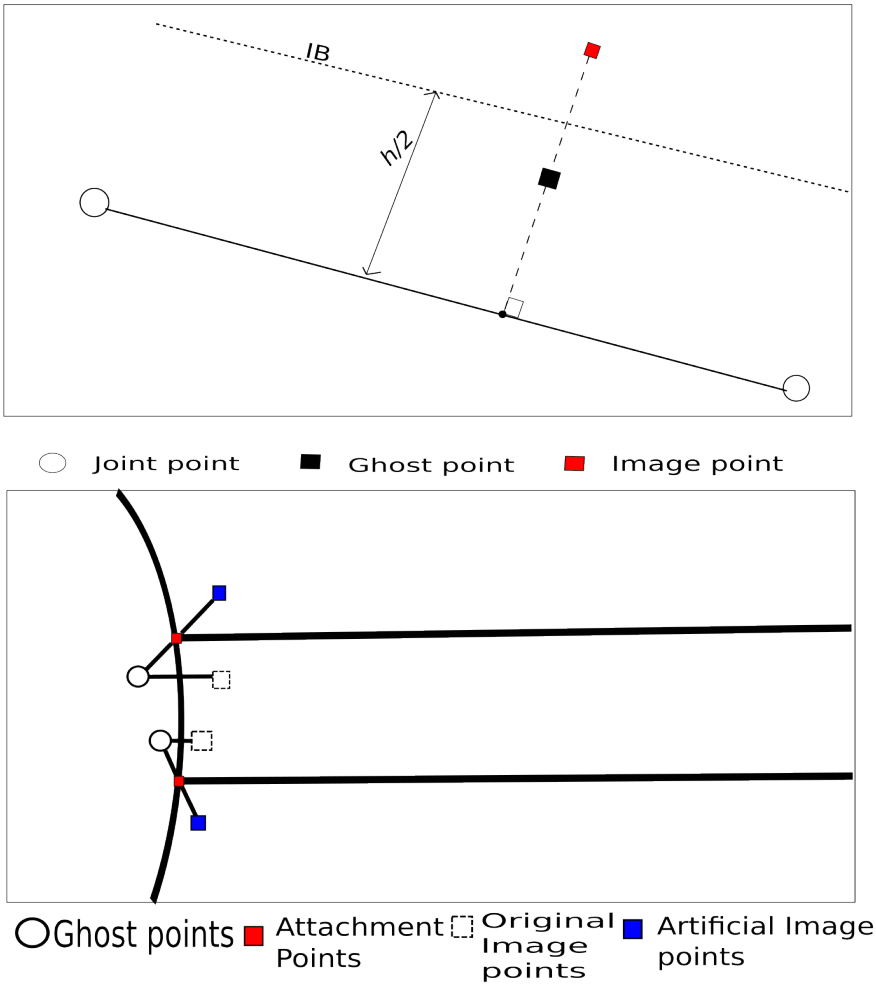

Figure 3.5: (Upper) Illustration of the artificial plate thickness added along the normal of the center line on its upper side and how the image point is found. (Lower) Illustration of the ghost points near the attachment of the plate at the circular cylinder are treated.

plate thickness. The round trailing edge of the plate can be seen in Figure 3.6.

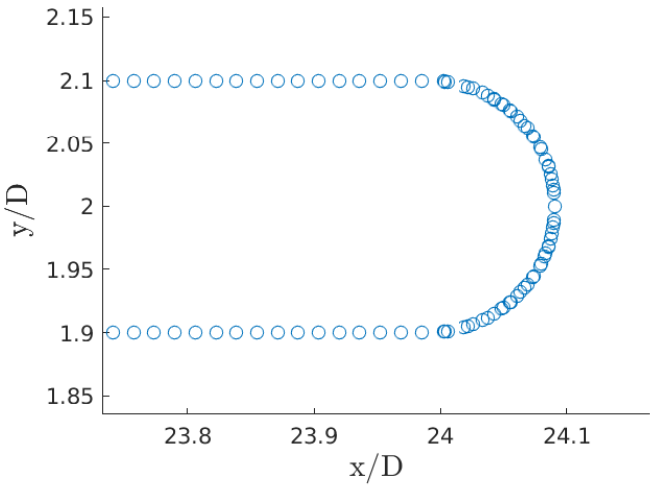

Figure 3.6: Scatter plot of the boundary intersection points near the plate trailing edge for an elastic plate behind circular cylinder. The boundary intersection points are the points where the immersed boundary method imposes the boundary conditions.

Information is transferred between the systems through the ghost points and their closest joint points. The velocity of the structure at a joint point *i* is $v_y^{(i)}(t) = \frac{ds_y^{(i)}}{dt}$, where s_y is the second component of the joint point vector **s**, i.e., the displaced y-coordinate of the center line. This velocity is given to all ghost points that have joint *i* as its closest joint point and is imposed as a boundary condition at the immersed boundary. To find the pressure load on the structure at joint number *i* the pressures at ghosts points that have joint *i* as its closest joint point are identified. Since the Neumann condition for pressure (3.5) is imposed the pressure at the image point is the same as that at the ghost point. This means summation over the ghost points is the same as summation over the image points. The pressure at the ghost points which lie above the plate, i.e., have a positive y-component with respect to the centerline are averaged to find the upper pressure $p_{\text{upper}}^{(i)}$ at this joint point. The same is done for the ghost points that lie below the plate i.e., have a negative y-component with respect to the centerline, to find the lower pressure $p_{\text{lower}}^{(i)}$. The pressure load imposed at joint *i* can then be calculated as: $\delta p^{(i)} = p_{\text{upper}}^{(i)} - p_{\text{lower}}^{(i)}$.

The pressure difference at the end of the plate, point number *m*, is extrapolated from the last four neighboring points, $\delta p^{(m)} = \frac{1}{4}\Sigma_{j=1}^{4}\delta p^{(m-j)}$. This was due to large errors that appeared upon summation over the plate trailing edge. Due to problems with the pressure interpolation, setting $\delta p^{(m)} = \delta p^{(m-1)}$ gave more unstable solutions than this 4 point averaging for the trailing edge pressure difference.

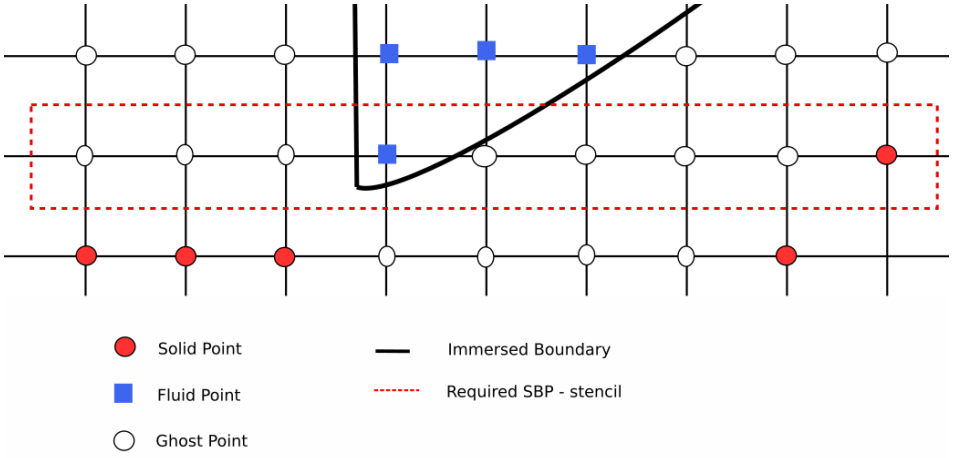

Figure 3.7: Illustration of the required SBP-boundary operator stencil width being wider than the number of available points.

Issues and solutions

a) *Concave corners with too few fluid points*
To exploit the stability properties of the summation by parts (SBP) method, the SBP differencing operator is used. At the immersed boundary viscous flux vectors $\vec{F}^v$ and $\vec{G}^v$ are also determined at the three layers of ghost points. The SBP operator applied at these ghost points and neighboring fluid points will, however, require a locally wider stencil where 12 points are required to evaluate the derivatives. This causes a problem where the immersed boundary meets sharp corners such as illustrated in Figure 3.7. In this illustration, the required 12-point stencil width is not available, as only 8 fluid or ghost points are present on the middle grid line in the x-direction. This problem appears near the intersection of the plate and the cylinder surfaces. To remedy this the plate is held flat near the intersection, i.e., $s_y^{(j)} = s_y^{(1)} = 0, j = 2, ..., N$, where $s_y^{(1)}$ is the displacement of the first joint point, and N is the number of points held in place. N depends on the density of the plate points compared to the grid density, in these simulations $N = 20$ was chosen. This assumes that the x- derivative of the displacement is equal to zero near the plate cylinder intersection. This assumption also corresponds to the boundary condition for the Euler-Bernoulli structure model. This assumption is also reduced when grid point density is increased as a smaller length of the plate has to be held in place.
b) *Third ghost points without enough neighboring ghost points*
As mentioned above, at least 12 points are required to evaluate the derivatives of the viscous flux vectors $\vec{F}^v$ and $\vec{G}^v$ at the immersed boundary. In certain situations, small perturbations created regions without enough ghost or fluid points to define these derivatives. These situations appeared more frequently near the flat plate configuration, as a small perturbation from the zero displacement line could cause jumps in the ghost point configuration. Such a situation is illustrated in Figure 3.8. The solution to this issue was to calculate the local derivatives with the number of points available with non-SBP methods

if less than 12 points were available. These derivatives were calculated with the second-order central difference scheme where three points were available, the first order one-sided scheme where two points were available. Certain situations arose were only one point was available to evaluate the derivative. To ease the implementation the local derivative was set to zero at those points. These problems only occur at the third ghost point from the immersed boundary and therefore can only interact with the flow through how this changes the viscous fluxes. A discussion of these effects can be found in section 4.3.

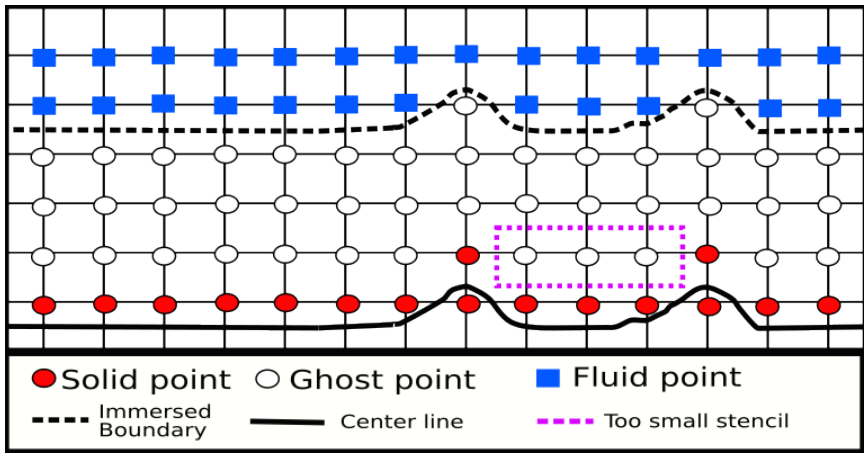

Figure 3.8: Illustration of a region with too few neighboring ghost points to determine the $\xi-$ derivatives of u, v, T in the viscous fluxes.

Chapter 4

Results

4.1 Simulation setup

Two cases of FSI problems are considered. An elastically mounted circular cylinder in crossflow demonstrates our immersed boundary method's capabilities to capture rigid body fluid-structure interaction. The modeling of such a system has applications for structure problems where vibration due to periodic vortex shedding is of interest. Vortex-induced vibrations is a problem with large interest from the petroleum industry due to its applications for drilling risers [54]. These vibrations cause fatigue damage on the structures which can endanger safe and continued operation [21]. These vibrations are caused by the structure interaction with the shed vortexes and can involve complex vortex patterns.

A circular cylinder with an attached elastic plate was implemented to investigate this IBM's ability to capture FSI-problems with deforming structures. Proper modeling of elastic plates and beams is a challenge in many engineering applications. Fluid-structure interaction of deformable plates is used for hydrodynamic simulations for marine applications [49][10] as well as biomechanical modeling of the soft palate in the pharynx [28].

4.1.1 FSI of elastically mounted circular cylinder in freestream

This test case is taken from Yang and Stern [55], to verify our FSI method against their, cf. section 4.2. The circular cylinder is imposed as in [46] and [29] by the immersed boundary method. The cylinder with diameter D is centered at $x_0 = y_0 = 20D$, in a channel 90D long and 40D high. This domain is large enough to reduce boundary- and wave reflection effects [27]. Symmetry boundary conditions were imposed at the upper and lower boundaries. In this work, the in- and outflow boundary conditions are applied by injection of the Navier-Stokes characteristic boundary condition [44][29] as mentioned in section 3.2.1. Yang and Stern [55] used a smaller domain where the total domain was 40D long and 20D high. Yang and Stern [55] applied freestream condition at the top and bottom boundaries, freestream inlet condition and a convective outflow condition. As the boundaries are far from the cylinder and these boundary conditions are

expected to have little impact on the flow, these differences are assumed negligible when considering the near cylinder flow. The cylinder was held in place until non-dimensional time $t' = \frac{tc_0}{D} = 520$, when periodic vortex shedding had developed, as was done in [55]. The cylinder was then released and allowed to interact with the flow as an elastically mounted cylinder modeled as a mass-spring-damper system.

The same grid as considered in [46] was used, described there as follows: "The solutions were calculated on a 441x261 grid, with 115101 grid points in total. The domain is structured by blocks, where the block with the cylinder had the finest grid. The nine blocks are used for the parallelization of the flow solver, this is described in [29]. In the block containing the cylinder, a fine grid spacing of (Δx=Δy=$D/50$) was used. The grid spacing is smoothly stretched to ($\Delta x \approx \Delta y \approx D/2$) near the domain boundaries." [46] Two grid refinements were considered, one corresponding to grid size $\Delta = \frac{D}{25}$ near the cylinder and the other refined with twice as many grid cells in the whole domain, corresponding to grid spacing $\Delta = \frac{D}{50}$ near the cylinder. The grid is presented in Figure 2.1.

4.1.2 FSI of cylinder with attached elastic plate in channel flow

A circular cylinder with diameter D is placed in a channel with its center locked at position $x_0 = 20D, y_0 = 2D$. The channel domain considered is a long 2D channel with length $L = 90D$ and height $H = 4.1D$. Attached on the right of the cylinder is a flexible plate with thickness $h = 0.2D$ and length $l = 3.5D$. The end point of the plate will be referred to as point A and is used for comparison with previous results, cf. Figure 4.1. The physical geometrical sizes introduced in [52] are presented below in Table 4.1.

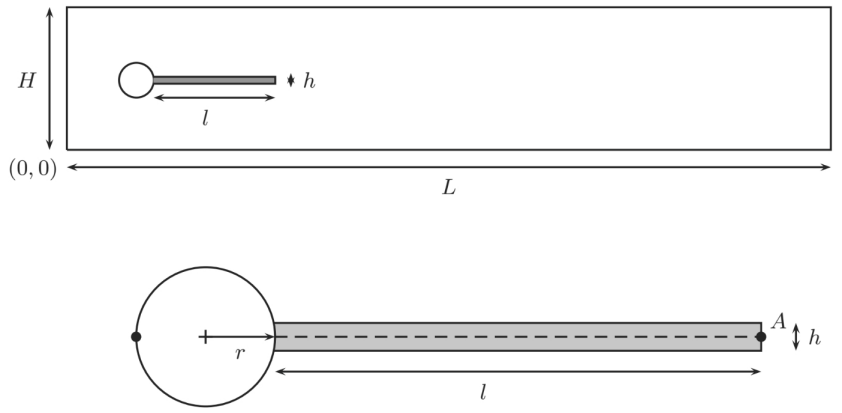

Figure 4.1: Illustration of computational domain (above) and structure details (below), taken from [52].

The plate is held in place until dimensional time $t = 1[\text{sec}]$ such that the initial condition would not affect the simulations. The initial conditions in the entire domain correspond to $U(x, y, t = 0) = 0$.

Table 4.1: Geometric dimensions as used in [52], except for L, which was L=2.5 in [52].

D	0.1 [m]
L	9.0 [m]
H	0.41 [m]
h	0.02 [m]
l	0.35 [m]
x_0	0.2 [m]
y_0	0.2 [m]

The equations of fluid motion are transformed from Cartesian coordinates into transformed coordinates described in section 2.3. The transformation gives a finer grid near the cylinder and plate as to properly capture the near structure dynamics. Near the structure the grid spacing is $\Delta = \frac{D}{100}$, the grid is then stretched according to the transformation given in [29] to approximately a grid spacing of $\Delta x \sim \frac{D}{20}$ near the inlet and $\Delta x \sim \frac{D}{2}$ near the outlet. The grid was stretched to a grid spacing of $\Delta y \sim \frac{D}{50}$ near the top and bottom walls. To compare with [52], no-slip, adiabatic temperature boundary conditions with the boundary layer approximation for the pressure were applied at the top and bottom boundaries. The inlet velocity profile was imposed according to [52] written in dimensionless form as:

$$u_0(y^*) = 1.5\text{Ma}\frac{4}{(\frac{H}{D})^2}y^*(\frac{H}{D} - y^*), \tag{4.1}$$

where y^* is the non-dimensional y-coordinate $y^* = \frac{y}{D}$, Ma $= \frac{\bar{U}}{c_0}$, where $\bar{U}$ is the mean inflow velocity. Similar to [52] the imposed velocity profile was progressively introduced by a transient increase from zero to u_0:

$$u(0, y, t) = \begin{cases} u_0(y)\left(\frac{1-cos(\frac{\pi}{2}t)}{2}\right), & \text{if } t \leq 2\text{[s]} \\ u_0(y) & \text{otherwise} \end{cases} \tag{4.2}$$

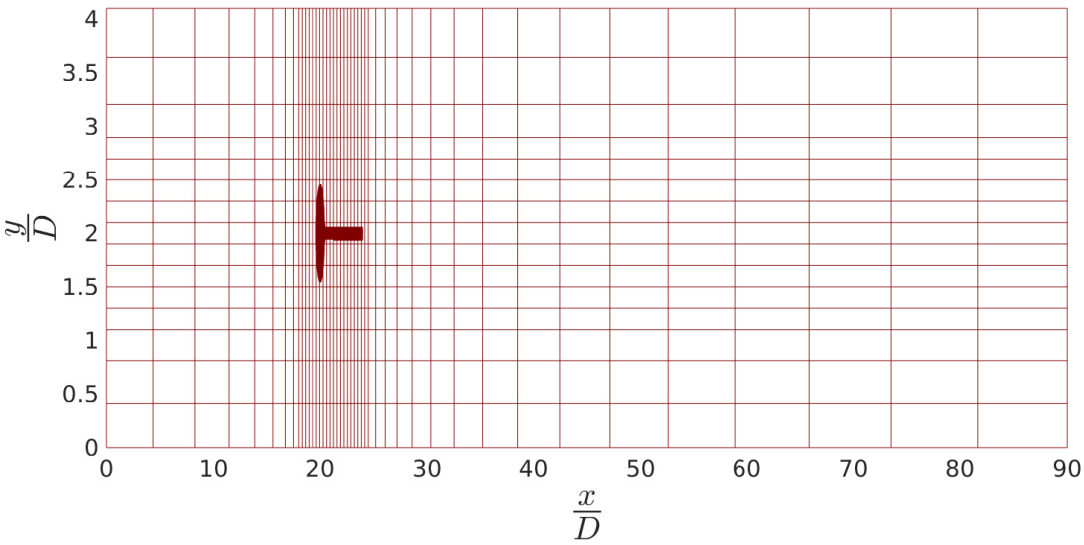

Figure 4.2: Grid for FSI of circular cylinder with attached elatic plate in channel flow. The darker shape is the circular cylinder with attached plate. Cartesian grid near the cylinder for $(x, y)\epsilon$[18D, 24.5D]x[1D, 3D] with local grid spacing $\Delta = \frac{D}{100}$, and stretched grid away from the cylinder. Every 10th line is plotted.

4.2 Elastically mounted cylinder

The elastically mounted circular cylinder in crossflow was simulated at Reynolds number Re=200, Ma=0.25 as to be comparable with the results of Yang and Stern [55] and Blackburn and Karniadakis [6]. The flow was simulated with air at standard conditions as the fluid. The flow was simulated as two-dimensional laminar flow, with no turbulence model implemented. The Reynolds number 200 is near the limit of what the 2D Navier-Stokes equations can accurately predict, as it is near the transition to turbulence. For further discussion of this see [46].

The cylinder was initiated at position (20D,20D), which was chosen as the equilibrium position of the mass-spring-damper system. As described in section 4.1.1, the cylinder was held in place until non-dimensional time $t' = \frac{tc_0}{D} = 520$, when vortex shedding had developed for the fine grid solution. For the unrefined solution with grid spacing $\Delta x = \Delta y = \frac{D}{25}$ near the cylinder, the vortex shedding had not fully developed. However, at the time of release, the cylinder was quickly accelerated in the x-direction due to drag forces. This appears to have initiated the vortex shedding. This can be seen in Figure 4.12, as both systems appear to have reached the same periodic state these results at grid spacing $\Delta = \frac{D}{25}$ were used for comparison. The nondimensional time step was set to $\Delta t' = \Delta t \frac{c_0}{D} = 8 \cdot 10^{-3}$, corresponding to Courant number, $C = 0.48$ and $C = 0.24$ for the fine grid $\Delta = \frac{D}{50}$ and the coarse grid $\Delta = \frac{D}{25}$, respectively. Convergence is further discussed in section 4.2.3.

4.2.1 Comparison with previous results

The test case was set up to be comparable to the simulations of Yang and Stern [55], where the same system of structure equations was solved with an IBM incompressible flow solver. The parameters of equation (2.16) were set in accordance with [55] as $U^* = 5$, $\zeta = 0.01$ and $m^* = \frac{4}{\pi}$. The results in this section are from simulations where a simultaneous 4-stage Runge-Kutta solver was used for the time integration of the system, cf. section 3.2.2. The results of these simulations are presented below in Figures 4.3 and 4.4. Figure 4.3 shows the periodic motion of the cylinder after a periodic solution was reached. The axis of Figure 4.3 is shifted so that x=0 matches the point where the trajectory crosses itself in the $x-$direction. This point corresponds to the center of the figure eight oscillations. The frequency of the oscillation are $f_y = 14.9[Hz]$, and $f_x = 30.0[Hz]$, where subscript indicate the direction of oscillation. To compare with previous results the frequency was non-dimensionalized with $f_0 = \frac{1}{t_0} = \frac{U}{D}$. The dimensionless frequency in the y-direction was found to be $f_y^* = 0.181$, where $f_y^* = \frac{f_y D}{U_\infty}$, which is the Strouhal number, *St* [3]. This result is in quite good agreement with [55] where the observed frequency was $f_y^* = 0.187$. The observed frequency lies very close to the observed vortex shedding frequency of the released cylinder, $St = 0.182$, meaning that the oscillations synchronize with the vortex shedding frequency. The observed vortex shedding frequency before cylinder release was $f_{\text{unreleased}} = 0.190$. The frequency of oscillation in the x-direction was $f_x^* = 0.364$ for the fine grid solution $\Delta = \frac{D}{50}$, the frequency was lower for the coarser grid with $\Delta = \frac{D}{25}$ where the frequency was found to be $f_x^* = 0.360$. In the y-direction the same oscillation frequency was observed for both grids.

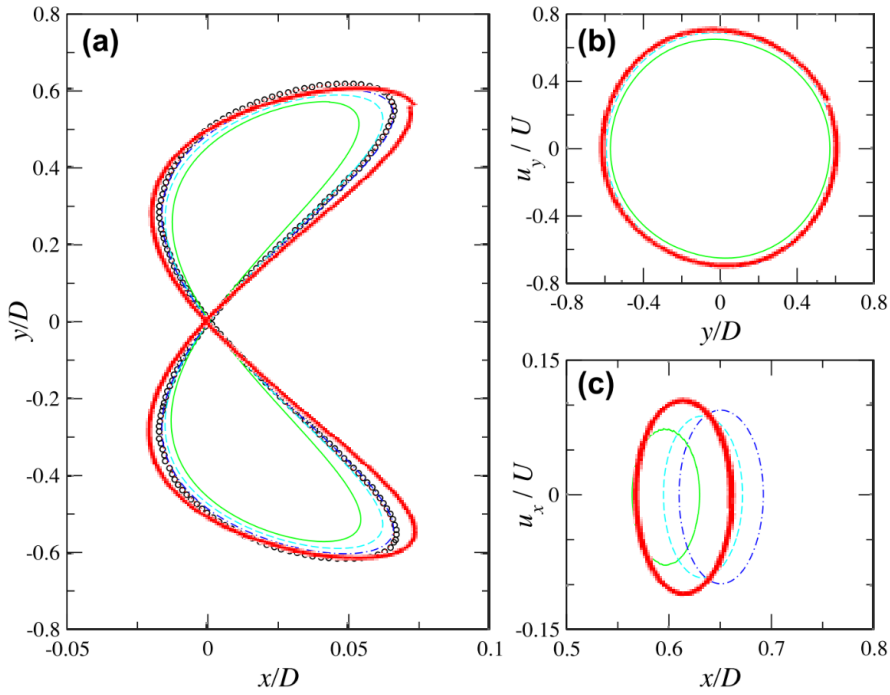

Figure 4.3: Comparison of the cylinder centerline trajectory (left plot) and the cylinder velocity components phase plots (right plot) for elastically mounted circular cylinder at Re=200, Ma=0.25, m*=$\frac{4}{\pi}$. Figures taken from [55] and overlayed with present results.
Green solid line: Yang and Stern [55] results with a coarse grid (160x120 grid points)
Cyan dashed line: Yang and Stern [55] results with a medium grid (320x240 grid points)
Blue dashed-dotted line: Yang and Stern [55] results with a coarse grid (640x480 grid points)
Black circles (o): Blackburn and Karniadakis [6](only left plot)
Red sold line : Present fine grid ($\Delta = \frac{D}{50}$) and ODE and PDE simultaneously solved with RK4.

Figure 4.3 (left) shows that both the present and previous simulations appear to create the same periodic motion, a slanted figure eight shape. Previous results appear to converge towards a solution upon grid refinement, this is also observed in present results, which is discussed in section 4.2.3. The results using a coarser grid and the explicit Euler method with a fine $\Delta = \frac{D}{50}$ and coarse $\Delta = \frac{D}{25}$ grid is also present in section 4.2.3.

The present method has previously been investigated in [27] and [46]. From these investigations, the IBM appears to underestimate the drag coefficient compared to other numerical results, while it appears to better approximate experimental results [46]. In Ringstad [46], the lift coefficient was found to be in better agreement with other numerical results. Figure 4.3 (lower right) show that the center of oscillation for the finest grid solution of [55] is about $x_c = x_0 + 0.651D$, where x_c is the center of oscillations. The present results place the center of oscillation further upstream at $x_c = x_0 + 0.616D$. The present results are therefore in better agreement with the results of Blackburn and

Karniadakis [6], where the center of oscillation was $x_c = x_0 + 0.62D$. The trajectory of the cylinder is wider in the $x-$ direction for the present method than those of [55][6]. This indicates that either the drag forces or the solution of the structure equations differ between the present and previous work. The present results with the classical explicit Runge-Kutta method with a fine grid ($\Delta = \frac{D}{50}$) is compared to the results using a coarser grid ($\Delta = \frac{D}{25}$) and with the explicit Euler method for a fine and a coarse grid in Figure 4.13. For all methods and grid resolutions, the $y-$direction results match each other and previous results. The results in the $x-$direction match each other for the same grid resolution. This indicates that the method used to solve the structure-dynamics is not decisive for the results. This suggests that it is likely that different calculated drag forces are the reason for differing results. This supported by the fact that the drag force calculated by this IBM was lower than those of other numerical results for a stationary cylinder in cross-flow [46]. In the present results presented in Figure 4.3 (left) a jump in the trajectory near $(x/D = 0.75, y/D = 0.55)$ is observed. This is where the start and end of the last period of the simulation. This indicates that the solution is not fully converged in time.

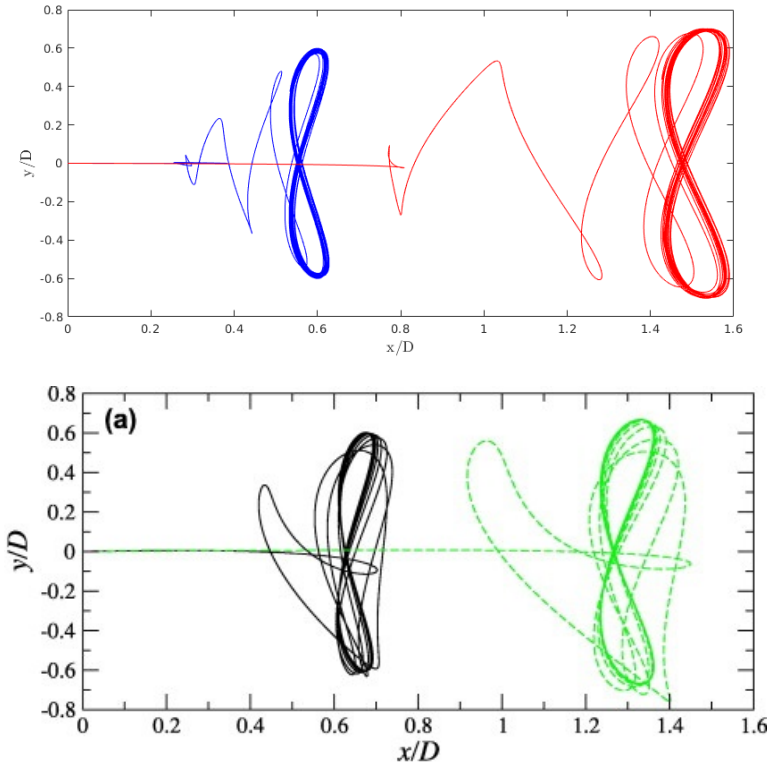

Figure 4.4: Cylinder centerline trajectory
x- and y-displacement from equilibrium position (0,0) for Re=200, Ma=0.25. $\Delta = \frac{D}{25}$, $m^* = \frac{4}{\pi}$ and $m^* = \frac{1}{2}$. (Upper) Present results, Red line: $m^* = \frac{1}{2}$, blue line: $m^* = \frac{4}{\pi}$ (Lower) Yang and Stern [55], Green line: $m^* = \frac{1}{2}$, black line: $m* = \frac{4}{\pi}$

The simulations were also performed with mass ratio $m^* = 0.5$, with the ODE (2.17) solved with the explicit Euler method and the Navier-Stokes equations solved with grid size $\Delta = \frac{D}{25}$. These simulations were initiated with the circular cylinder at position $x_0 = 19, y_0 = 20$ to keep the cylinder inside a single parallel block in the computational domain. From Figure 4.4 it is clear that the reduced mass moves the center of the oscillations further downstream. This effect is larger for the present simulations than that of [55]. The blue and black lines are the results with the higher $m^* = \frac{4}{\pi}$, these also differ location of the center of oscillation.

The instantaneous non-dimensional vorticity plot is shown in Figure 4.5. This shows the vortex shedding happens with the expected two alternating single vortices shed, which was also observed in [55]. These shed vortexes travel downstream in what is called a von-Karman vortex street. The vorticity of the flow field is defined with the Einstein summation convention as:

$$\omega_i = \epsilon_{ijk} \frac{\partial u_k}{\partial u_j}, \tag{4.3}$$

where ϵ_{ijk} is the Levi-Cevita symbol, i.e., =+1 if *(i,j,k)* is an even permutation, -1 if it is an odd permutation, and 0 if any index is repeated [38].

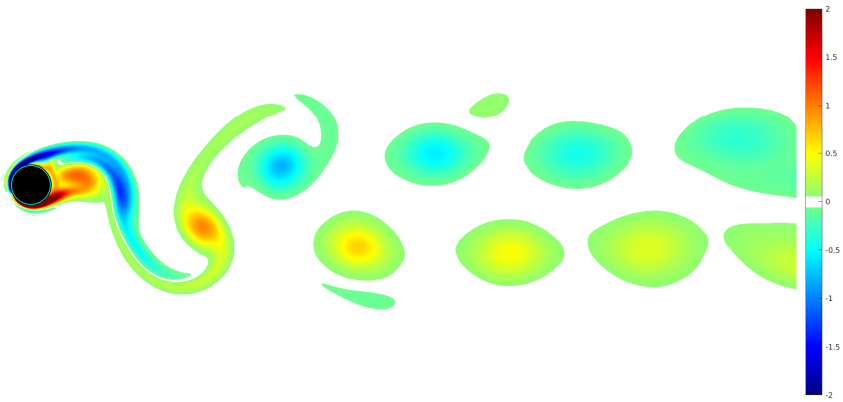

Figure 4.5: Instantaneous vorticity ω_z of the dimensionless velocity field $\vec{u}/c_0$ for an elastically mounted circular cylinder at Re=200, Ma=0.25, m*=$\frac{1}{2}$

It was also of interest to investigate sound propagation. By looking at the *pressure fluctuation* defined as:

$$p_{fluctuation} = p' - \bar{p}, \tag{4.4}$$

where $p' = \frac{p}{\rho_0 c_0^2}$, and $\bar{p}$ is defined as:

$$\bar{p}(x,y) = \frac{1}{t_2 - t_1} \int_{t_1}^{t_2} p(x,y,t)dt, \tag{4.5}$$

where t_1 and t_2 are the time instants of one period of cylinder oscillation.

This is shown in Figure 4.6, the average pressure of eqn. (4.5) was averaged over three full oscillations of the cylinder.

Figure 4.6 shows that the main pressure fluctuations at this Reynolds number are due to the von-Karman vortex street following the cylinder [8]. The imposed boundary conditions create reflecting pressure boundary conditions. The pressure waves that are reflected off the top and bottom walls are suspected to bounce off the wall and interfere with the established pressure waves caused by the von Karman vortex street.

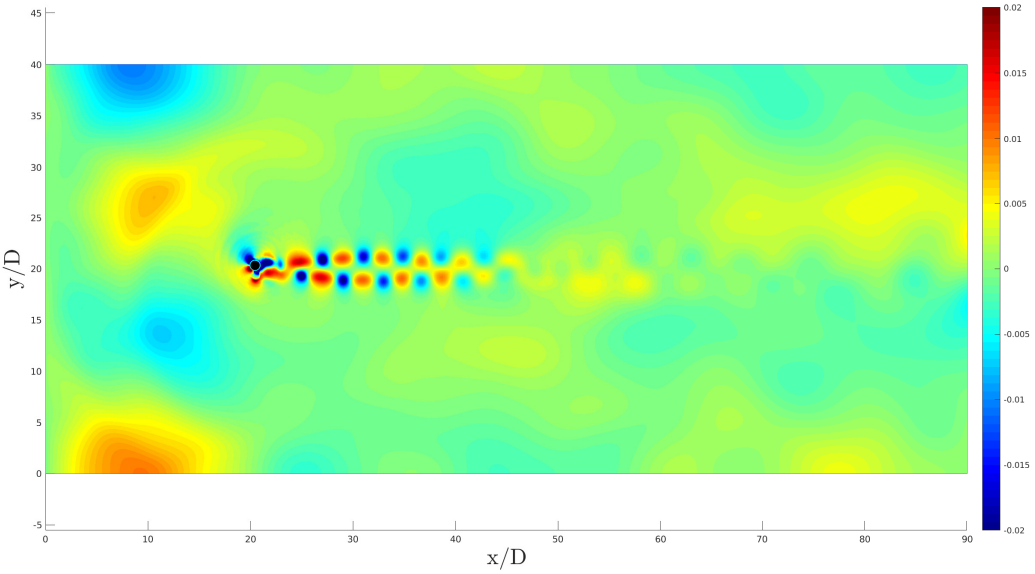

Figure 4.6: Dimensionless fluctuation pressure, eq. (4.4) for Re=200, Ma=0.25, $\Delta = \frac{D}{25}$, $m^* = \frac{1}{2}$

4.2.2 Energy exchange

The energy exchange between the flow and the structure is investigated. The rate of energy lost from the flow to the structure can be expressed in the form:

$$P = \int_{\partial\Omega} (pn_j u_j - n_j u_i \tau_{ij}) dA = uF_D + vF_L, \tag{4.6}$$

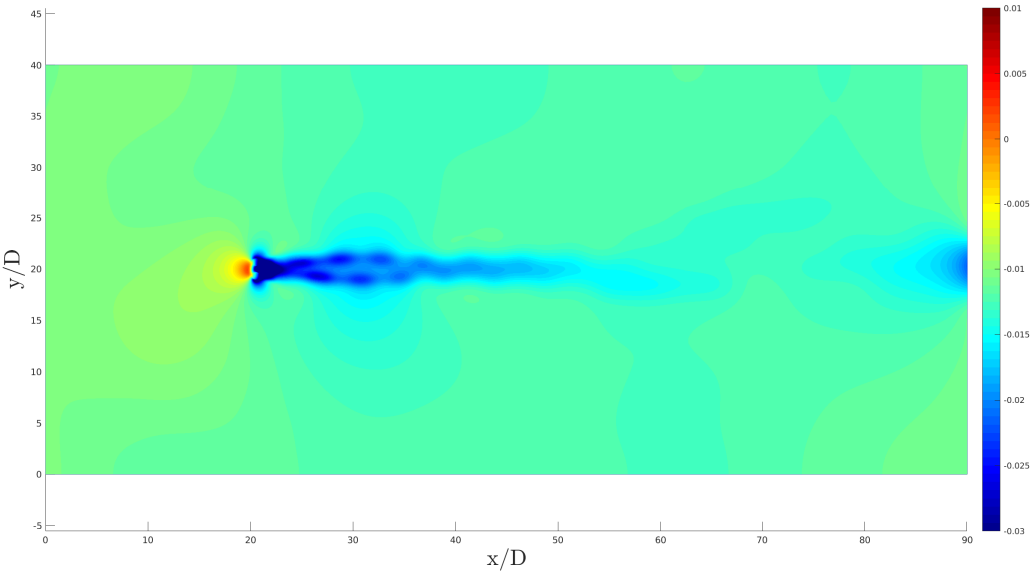

Figure 4.7: Dimensionless average pressure, eq. (4.4) for Re=200, Ma=0.25, $\Delta = \frac{D}{25}$, $m^* = \frac{1}{2}$

where $\partial\Omega$ is the boundary interface between the fluid and the structure, n_j is the *j*-th component of the unit normal vector pointing into the structure, F_D and F_L are the lift and drag forces, u and v the velocity components of the moving structure, P is the rate of work exerted from the fluid flow on the structure. For these simulations, the adiabatic boundary condition was applied. Thus, no heat is transferred between the structure and the fluid. This energy transfer at the interface can be recovered in the structure model by considering the forcing terms $F_D(t)$ and $F_L(t)$ in equations (2.14) and (2.15), respectively. By regarding the total energy of the structure system:

$$E_{tot} = \frac{1}{2}(kx^2 + m\dot{x}^2 + ky^2 + m\dot{y}^2), \tag{4.7}$$

the rate of change of energy with time can be derived from differentiation and inserting equations (2.14) and (2.15) for the terms $m\ddot{x}$ and $m\ddot{y}$, respectively. This yields:

$$\frac{\partial E_{tot}}{\partial t} = F_D u + F_L v - b(u^2 + v^2). \tag{4.8}$$

The term $-b(u^2 + v^2)$ is the rate of energy removal through the damping term $-bu$ and $-bv$ in equations (2.14) and (2.15), respectively, that removes energy from the system. From this it is evident that the same energy removed from the fluid system is analytically added to the structure system as the same energy transfer terms, $F_D u + F_L v$, appear in both equations. The energy transfer from the fluid to the structure, $F_D u + F_L v$, will be

referred to as the rate of added energy to the system. The energy lost through damping in the harmonic oscillator is lost from both systems as it is not regained in the fluid model. This rate of energy loss must be modeled as additional heating of the structure to maintain the physical rate of energy conservation. The rate of added and lost energy over time

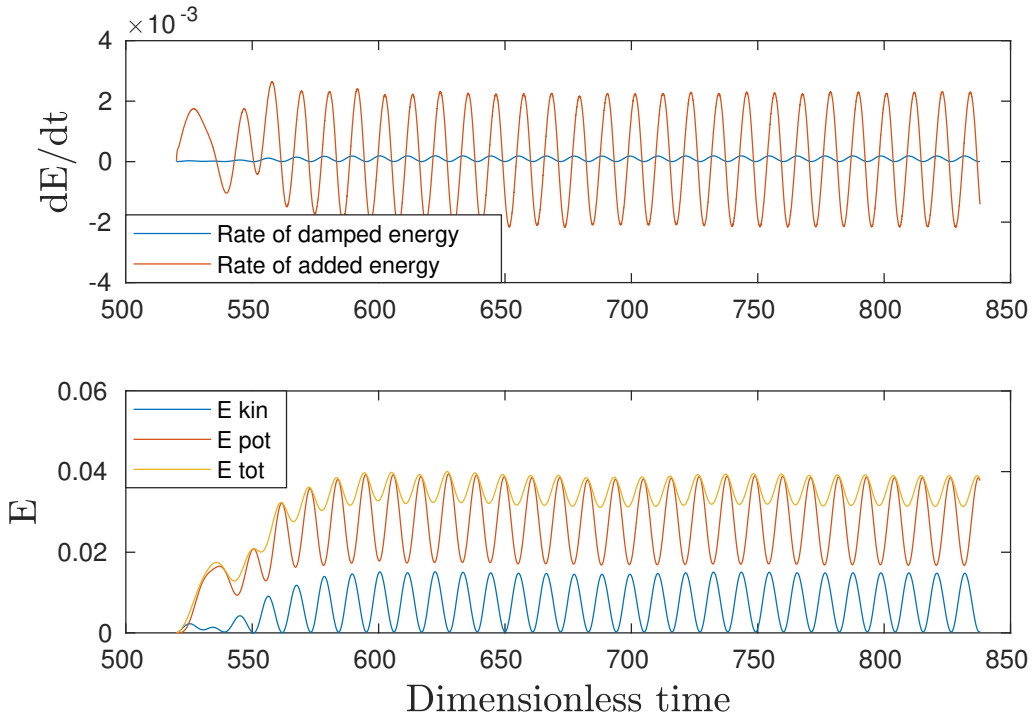

Figure 4.8: (Upper) Dimensionless power, $\frac{\dot{E}}{\rho_0 c_0^2}$ added and lost by the structure ODE over dimensionless time. (Lower) Total, kinetic and potential dimensionless energy $\frac{E}{\rho_0 c_0^2}$ of the cylinder over dimensionless time $t' = \frac{tc_0}{D}$. Re=200, Ma=0.25, $\Delta = \frac{D}{50}$, m*=$\frac{4}{\pi}$

in eq. (4.8) is shown in Figure 4.8 (upper). This shows that the damped energy rate, $-b(u^2+v^2)$, is dominated by the energy exchange done by the external forces to and from the cylinder. Figure 4.8 (lower) shows how the total energy is partitioned to the kinetic and potential energy. In this system the kinetic energy is defined by $E_{\text{kin}} = \frac{1}{2}m(\dot{x}^2 + \dot{y}^2)$ and is the energy stored in the movement of the cylinder. The potential energy is defined by $E_{\text{pot}} = \frac{1}{2}k(x^2 + y^2)$. It is the potential energy stored in the spring due to compression or extension of the spring. The total energy is defined as the sum of the potential and kinetic energy, cf. equation (4.7).

Most of the total energy in the mass-spring-damper system is stored as potential energy. This is due to the static displacement of the cylinder at the center of oscillation. To investigate the conservation of the energy the power to the mass-spring-damper system, eqn. (4.8), was integrated from $t = 0$ to $t = t_{end}$ using the trapezoidal rule. This should

analytically match the total energy in the system, eqn. 4.7. These do not exactly match and the numerical error in conservation was estimated as $E_{\text{err}} = E_{\text{tot}} - \int_0^{t_{end}} \frac{\partial E_{tot}}{\partial t} dt$. From this error estimate, it was shown that the error is relatively small, $err \sim 2\%$ of the total energy, at non-dimensional time $t_{end} = 830$.

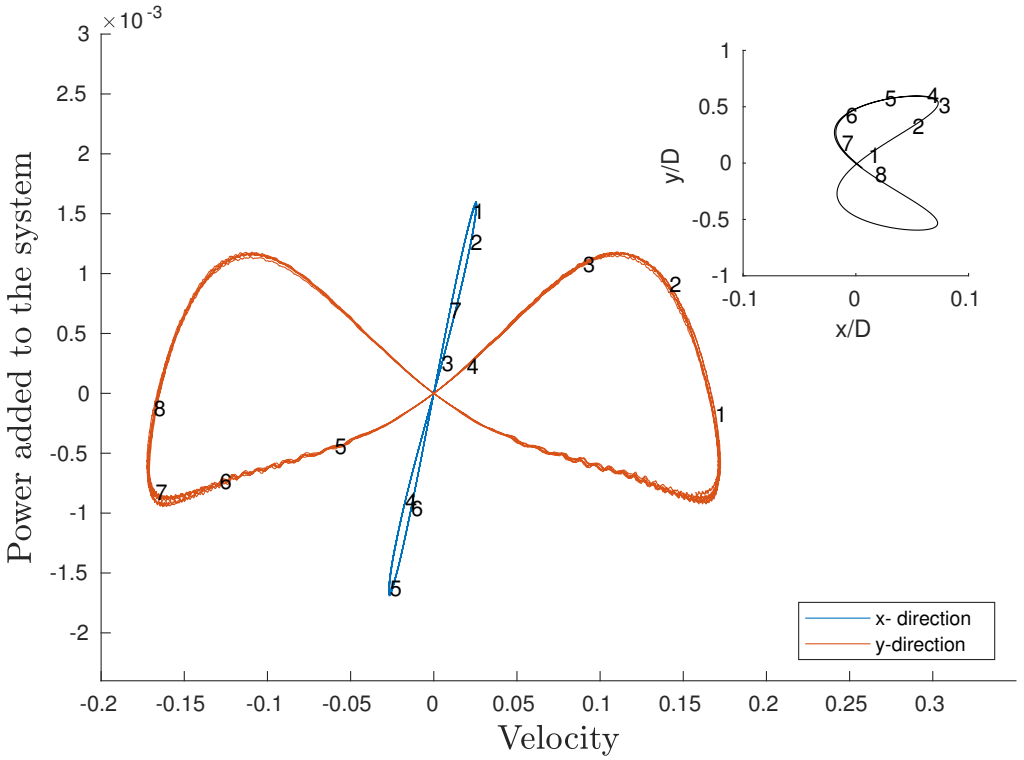

Figure 4.9: (Main) Dimensionless power added at different cylinder velocities. (Upper right) The corresponding position at different time intervals 1-8 during the cylinder trajectory. Re=200, Ma=0.25, $\Delta = \frac{D}{50}$,m*=$\frac{4}{\pi}$.

This analysis is furthered by looking at how the energy is transferred between the systems when periodic oscillations are reached. By looking at the added power, $F_D u + F_L v$, at different velocities the pattern of rate of energy transfer can be found. This can be seen in Figure 4.9. The added power in the *x*- and *y*-directions are separated and shown plotted against the velocity components *u* and *v*, respectively. To relate these velocities to their corresponding positions along the cylinder centerline trajectory at evenly spaced time-intervals an additional plot is added in the upper right of this Figure. These points are shown for one upper loop of the cylinder centerline trajectory and are symmetric about the lower loop. Intuitively, the added and removed power must sum to zero during one whole loop of the trajectory, else the solution energy will grow with time. This can readily be seen for the *x*-direction as the rate of energy added is symmetric about the zero-power

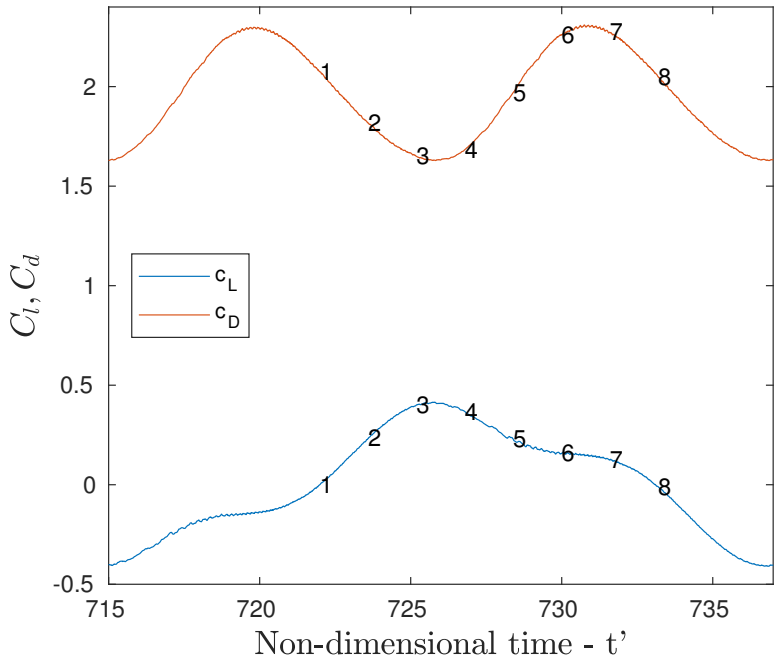

Figure 4.10: The time developement of the lift and drag coefficients for the explicit Euler method at $\Delta = \frac{D}{50}$, Re=200, Ma =0.25, $m^* = \frac{4}{\pi}$. The time intervals of Figure 4.9 are included.

axis.

In the x-direction, the most power is transferred near the midpoint between the two extremes in x-position, i.e., at points **1** and **5**. Point **1** corresponds to the most positive added power. Here the drag force and the x-velocity coincide at the point of maximum velocity. In this region, the fluid is exerting forces on the cylinder, this power is transferred over time into the spring's potential energy. The spring force slows down the cylinder up to point **3**. From point **3** to **5** here the spring force accelerates the cylinder in the negative x-direction, opposing the drag forces from the fluid. This is exchanging the stored potential energy of the spring for kinetic energy, which in turn is transferred back to the fluid.

The rate of energy transfer between fluid and structure in the y-direction is more complex due to the variation of the lift coefficient. Starting from point **1** through **3** the lift force and v-velocities coincide as to increase the power to the system. At the peak y-position, near point 5, the spring pulls the cylinder down which opposes the lift forces exerted from the fluid. This continues until point **7**, as the cylinder reaches its most negative v-velocity. At this point, the lift coefficient switches from positive to negative due to the shedding of a vortex, cf. Figure 4.10. After this, the effect is symmetric to the rate of energy transfer from points **1**-**4**.

The noisy disturbances in Figure 4.9 near points **1**, **6** and **7** in the y-direction are suspected to be numerical errors. It is suspected that these occur near these regions as they

happen near the crossing point of the trajectory, i.e., where the cylinder has the highest velocity. As the energy transfer is largest for largest velocities, cf. eq. (4.8), the error is scaled to be larger for those regions. These numerical errors are investigated for different grid refinements in Figure 4.11. This is discussed further in section 4.2.3.

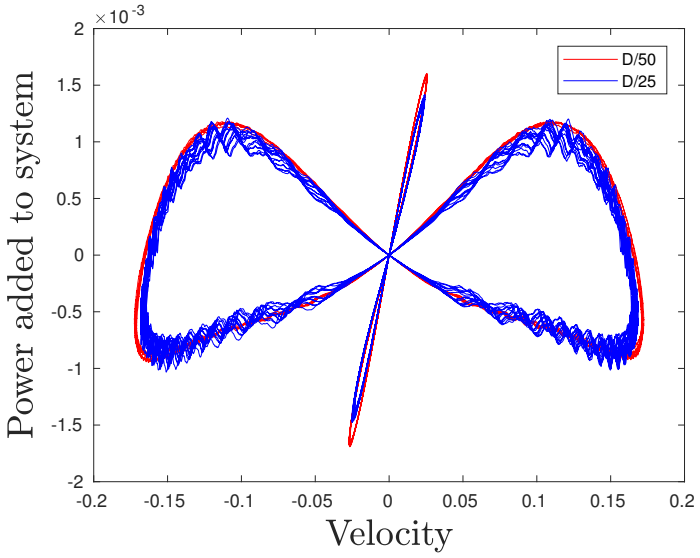

Figure 4.11: Dimensionless power added at different cylinder velocities. Re=200, Ma=0.25, m*=$\frac{4}{\pi}$, Blue; $\Delta = \frac{D}{25}$, Red; $\Delta = \frac{D}{50}$

4.2.3 Convergence

In Figure 4.3 the results of the simulations using the Runge-Kutta method with grid size $\Delta = \frac{D}{50}$ were compared to those of [55]. In this section, different methods and grid refinements for the same simulation are compared.

Two grid refinements have been investigated for this case, a grid spacing of $\Delta = \frac{D}{25}$ near the cylinder and a refined run with grid spacing twice refined to $\Delta = \frac{D}{50}$ near the cylinder. This was investigated for the explicit Euler method and the 4-stage Runge-Kutta method. The implementation of these methods are presented in pseudo-code *a)* and *b)* in section 3.2.4. These results are presented in Figure 4.13.

The present results indicate that the *y*-direction velocities appear to be quite well converged, cf. Figure 4.13 (upper right), both for the Runge-Kutta and the explicit Euler methods. This is also observed in the results by [55], cf. Figure 4.3 (upper right). On the other hand, the results of Yang and Stern [55] show that in the *x*-direction the center position is clearly shifting to the right upon grid refinement, cf. Figure 4.3(lower right). This trend is also observed for the present results. Both the Runge-Kutta method and the explicit Euler appear to converge toward the same fine grid solution.

As mentioned above the drag tends to be underestimated by this method compared

to other methods. The increased drag upon grid refinement is suspected to be caused by the better resolution of the boundary layer and through this an increase in friction forces. The trend of adding an increased mean drag force with grid refinement is evident from the time-history of the lift and drag coefficients presented in Figure 4.12. Here the drag coefficient of the refined solution is oscillating about a higher value. The

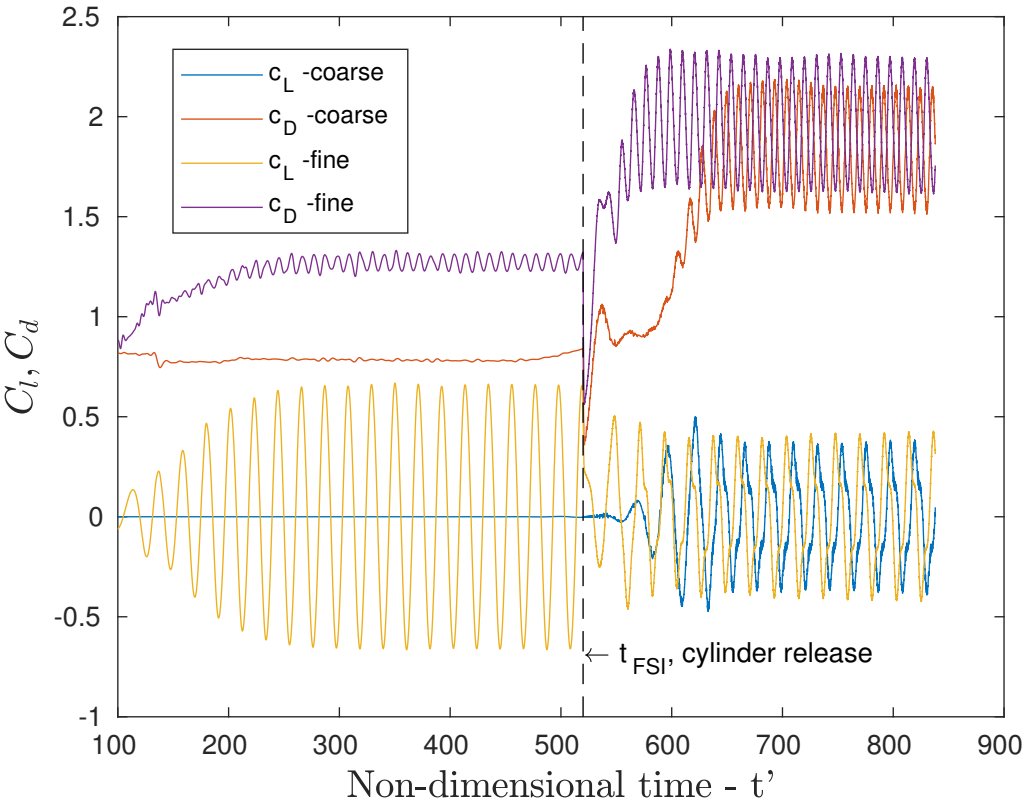

Figure 4.12: The time developement of the lift and drag coefficients for the explicit Euler method at $\Delta = \frac{D}{25}$ and $\Delta = \frac{D}{50}$, Re=200, Ma =0.25, $m^* = \frac{4}{\pi}$.

The numerical noise observed in Figure 4.9 mentioned above was investigated. The same plot is shown for both grid refinements in Figure 4.11. From this, it is clear that the noise is a numerical issue, as it is exacerbated by increased grid spacing. This indicates that a finer resolution than $\frac{D}{25}$ is required to inspect the rate of energy transfer properly.

It was concluded in [29] that this immersed boundary method was only properly resolved for a transversely oscillating circular cylinder at a grid spacing of the order $\Delta = \frac{D}{50}$. This is supported by the clear numerical noise generated at $\Delta = \frac{D}{25}$ in Figure 4.11. From previous work with this method [46], it was found that the IBM method shows only slightly above first-order convergence upon space- and time refinement for the lift and drag coeffi-

cients. However, the solutions in [46] might not have been run long enough to be conclusive. It was also found that due to stability restrictions a proper time refinement analysis was not achievable.

4.2.4 Numerical methods

Four different numerical methods were used to solve the system of ODEs (2.16). The numerical methods were investigated for two cases a) and b):

a) The system was initiated with zero velocity $\dot{x}(0) = 0$ and position from equilibrium $x(0) = x_0 = 20D$, and an external forcing of a sinusoidal drag force, $c_D(t) = A\cos(ft)$ was applied, where the force amplitude, A, was set to 100, and the frequency was set to $f = 10$.

b) The system was initiated with zero velocity $\dot{x}(0) = 0$ and an initial perturbation from the equilibrium position, $x(0) = x_0 + 0.2D = 20.2D$, where x_0 is the equilibrium position at $x = 20D$. No external forcing was applied, i.e. $c_D = 0$.

The simulations were run up to nondimensional end time $t_{\text{end}} = 100$ with time-step sizes $\vec{\Delta t} = \left[5 \cdot 10^{-5}, 1 \cdot 10^{-4}, 2 \cdot 10^{-4}, 4 \cdot 10^{-4}\right]^T \cdot 10^j$, for $j = 0, 1, 2$. Other simulations were done with higher frequency and longer simulation time, but these yielded very similar results. The mass-spring-damper parameters were set as described in section 4.2.1. As no analytic solution is available the results were compared to the finest time step solution with $\Delta t = 5 \cdot 10^{-5}$ referred to as the reference solution. The 2-norm is used to estimate the error of the different numerical methods. The 2-norm of the error is defined as $L_2 = \sqrt{\Delta t \Sigma (err)^2}$. The results are shown in Figure 4.14.

To investigate the order of accuracy the error is assumed to be of the form: $err(\Delta t) = C\Delta t^p$, where Δt is the time step size. The exponent of the error reduction is referred to as the order of the method, The L2-norm is used to estimate the error. To estimate the order of the temporal error reduction one can compare the errors after halving of the time step, $e\hat{r}r = \frac{err(\frac{\Delta t}{2})}{err(\Delta t)} \approx (\frac{1}{2})^{(p)}$. This can be solved for the order of the method, $p = ln(\frac{err(\Delta t)}{err(\Delta t/2)})/ln(2)$.

Table 4.2: Estimated order of convergence, p, for the different cases and methods.

Method	Forced oscillation	Free oscillation	Theoretical order
Explicit Euler	1.55	1.52	1
Størmer-Verlet	1.55	1.56	2
Heun's method	1.55	2.5	2
Runge-Kutta 4-stage	1.55	4.5 , 0.5 *	4

Figure 4.14 and Table 4.2 show that the investigated methods do not converge according to their theoretically expected order of accuracy, discussed below.

Forced oscillations

It appears that the forced oscillations impose a limit for the convergence rate of the methods, all the methods reach almost exactly the same order of convergence. Also, the errors

of Heun's method and the Størmer-Verlet method almost exactly overlap in Figure 4.14. It is not known why this upper limit is imposed on the system, but it is speculated that another error enters the equations and dominates the error. The only potential suspect is the external forcing. This would imply that this external forcing carries with it some upper limit to the convergence. These strange results could be indicative of a bug in the implementation of the methods.

Free oscillations

The more expected orders of these methods are found when the external forcing is removed from the equations and only free oscillations are considered. The Euler and Heun methods both converge at a rate slightly higher than their expected theoretical order, $p \sim 1.5$ and $p \sim 2.5$, respectively. The Størmer-Verlet method showed lower than second order convergence, reaching only order ~ 1.5. This is thought to be caused by the dependency on damping. As discussed in section 3.2.2 the low order observed for the Størmer-Verlet method is suspected to be due the velocity used in the damping term was taken from the intermediate stage $Q^{n+1/2}$. The Runge-Kutta method did not show a single consistent order of convergence for all time-steps and will be discussed in further detail. From Figure 4.14 the Runge-Kutta method shows slightly above the expected order of convergence for large time steps. However, at approximately $\Delta t = 10^{-2}$, the error is only reduced with order $p \sim 0.5$, meaning that a halving of the time step reduces the error by a factor of $\sqrt{2} \approx 1.414$. This sudden reduction in order indicates that the method reaches a point where further reduction of the time step is not significant for the method. This is thought to be an effect of round-off errors. An investigation of these effects using an exact solution for the reference solution is suggested for future work. The strange results are suspected to be caused by a programming error which was not found.

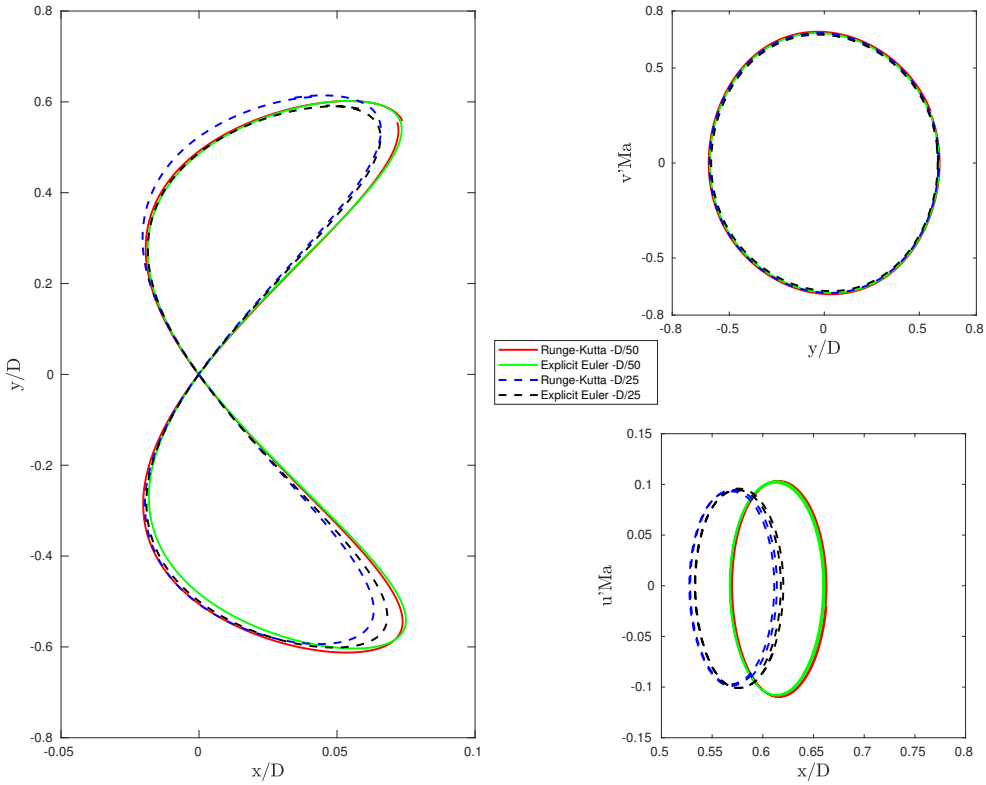

Figure 4.13: Comparison of the cylinder centerline trajectory (left plot) and the cylinder velocity components phase plots (right plot) for elastically mounted circular cylinder at Re=200, Ma=0.25, m*=$\frac{4}{\pi}$. Red solid-line: Runge-Kutta 4-stage method with $\Delta = \frac{D}{50}$ and Blue dashed-line: $\Delta = \frac{D}{25}$. Green solid-line: Explicit Euler method with $\Delta = \frac{D}{50}$ and Black dashed-line: $\Delta = \frac{D}{25}$.

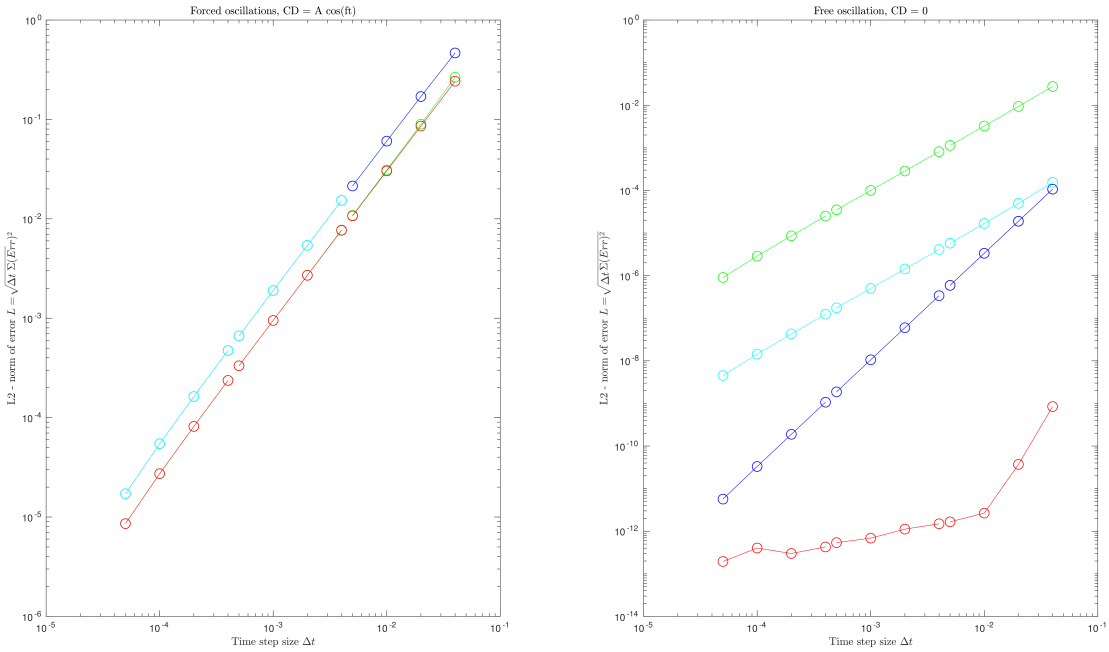

Figure 4.14: $\zeta = 0.01$ method = 1(cyan): Stormer-Verlet; method = 2(blue): Heuns; method = 3(green): Explicit Euler; method = 4(red): RK4

4.3 Elastic plate behind circular cylinder

Simulations of an elastic plate behind a circular cylinder were performed as to be comparable to the proposed FSI-benchmark by Turek and Hron [52]. A summary of the physical parameters of [52] is presented in Table 4.3.

The plate was initiated with displacements and velocity $s_y^{(i)} = \frac{d}{dt} s_y^{(i)} = 0$, for all plate points, i=1...m, where subscript indicate the component of **s**. The simulations were done with $m = 220$ joint points describing the elastic plate, corresponding to a spacing of the joint points comparable to $\Delta_s = s_x^{(i+1)} - s_x^{(i)} = \frac{l}{m} \approx \frac{D}{63}$, where *i* and $i + 1$ are two neighboring indices of the joint point vector **s**.

Geometrical and initial conditions were set as described in section 4.1.2. The parameters of the fluid and structure solvers were initially set according the benchmark, which is presented in Table 4.3. The parameters presented are the fluid density ρ_f, the fluid viscosity ν_f, the undisturbed fluid velocity U_∞, the flow Mach number $\text{Ma}_\infty = \frac{U_\infty}{c_0}$, the Reynolds number $\text{Re} = \frac{U_\infty D}{\nu}$, the structure mass density ρ_s, the structure elastic Young's modulus *E*, and the structure Poisson ratio ν_s. Two of the parameter settings proposed in [52] were tested, these are referred to as FSI1 and FSI2, respectively. These settings will be referred to as the reference settings. Turek and Hron [52] used an incompressible solver. In the present simulations, the Mach number was chosen such that the compressible effects were negligible. To speed up the simulations the speed of sound was artificially set to $c_0 = 1[\text{m/s}]$ and $c_0 = 3[\text{m/s}]$ for the test cases FSI1 and FSI2, respectively. This was set as to impose the Mach-number $\text{Ma} = 0.2$ and $\text{Ma} = \frac{1}{3}$ at the velocity scale U_∞ used in [52].

Table 4.3: Parameters set for the plate and fluid models in the benchmark of Turek and Hron [52], except ρ_s and ρ_f which were both set $\approx 10^3$ times higher in [52] at $10^3 \frac{\text{kg}}{\text{m}^3}$.

		FSI1	FSI2
ρ_f	$1 \frac{\text{kg}}{\text{m}^3}$	1.18	1.18
ν_f	$10^{-3} \frac{\text{m}^2}{\text{s}}$	1	1
U_∞	$1 \frac{\text{m}}{\text{s}}$	0.2	1
Ma_∞	-	0.2	1/3
Re	-	20	100
ρ_s	$1 \frac{\text{kg}}{\text{m}^3}$	1.18	11.8
E	$10^6 \frac{\text{kg}}{\text{ms}^2}$	1.4	1.4
ν_s	-	0.4	0.4

This structure model was investigated for this test case by Garcia [16] also using the Newmark method. Garcia [16] found that the structure model was able to accurately predict the movement of the plate.

The benchmark was simulated with an incompressible solver [52]. The present solver was, however, designed for gas dynamics. So the density of the fluid and the structure were both reduced by a factor of $\frac{\rho_f}{\rho_{\text{air}}}$, such that the gas density is set to ρ_{air}. This change was also done for the structure density as to keep the density ratio $\frac{\rho_s}{\rho_f}$ constant and in correspondence with the ratio of [52].

The results of the simulation of FSI1 is shown in Figure 4.15. This indicates that point A, the plate trailing edge is trending towards a displacement near $\phi_A/D \approx 7.67 \cdot 10^{-3}$,i.e. $\phi_A = 0.767 \cdot 10^{-3}$[m]. This is quite close to the results by [52] where the FSI problem reached a steady state solution with tip displacement $\phi_A = 0.821 \cdot 10^{-3}$[m]. Figure 4.15 indicates that the simulations had not yet reached steady state. However, they were ended early due to time constraints. Further simulation is required for a proper comparison with the results of the FSI-benchmark by Turek and Hron [52].

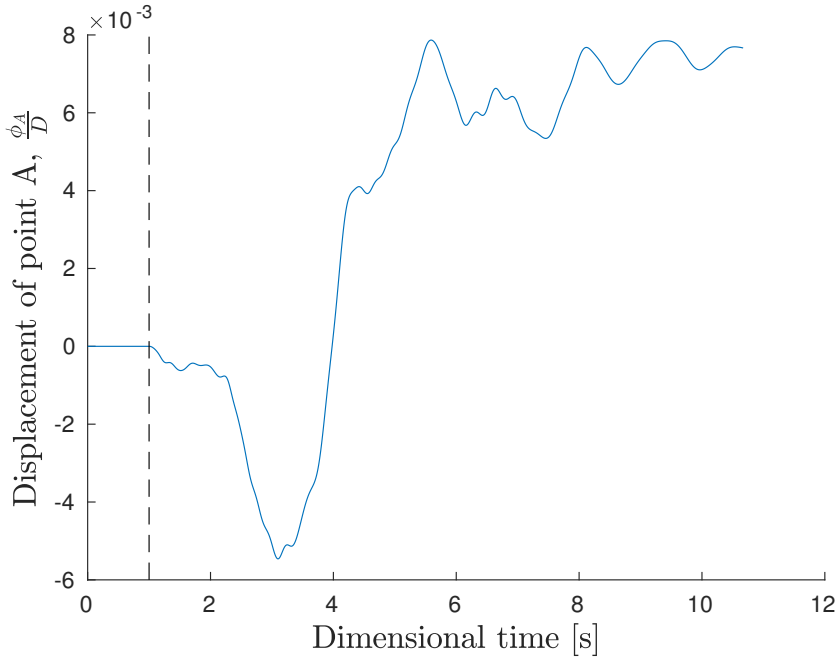

Figure 4.15: Displacement of point A $\frac{\phi_A}{D}$ over dimensional time, according benchmark test FSI1 of [52] for elastic plate behind circular cylinder, at Re=20, Ma =0.2. The dashed line indicates the time of release.

Figure 4.16 shows the dimensionless pressure near the cylinder plate arrangement for the case FSI1. Figure 4.16 shows the instantaneous vorticity of the dimensionless velocity field. No periodic motion is observed and a symmetrical solution about the plate is found. The symmetric and opposite vorticity above and below the cylinder is generated as the flow is forced around the obstructing cylinder. This vorticity is then carried with the flow across the plate and travels in a band of positive and negative vorticity down the flow. The vorticity near the top and bottom wall are due to vorticity generated by the boundary layer. The pressure is highest near the cylinder stagnation point. The pressure is reduced downstream in the channel as the pressure has to overcome the frictional forces at the walls.

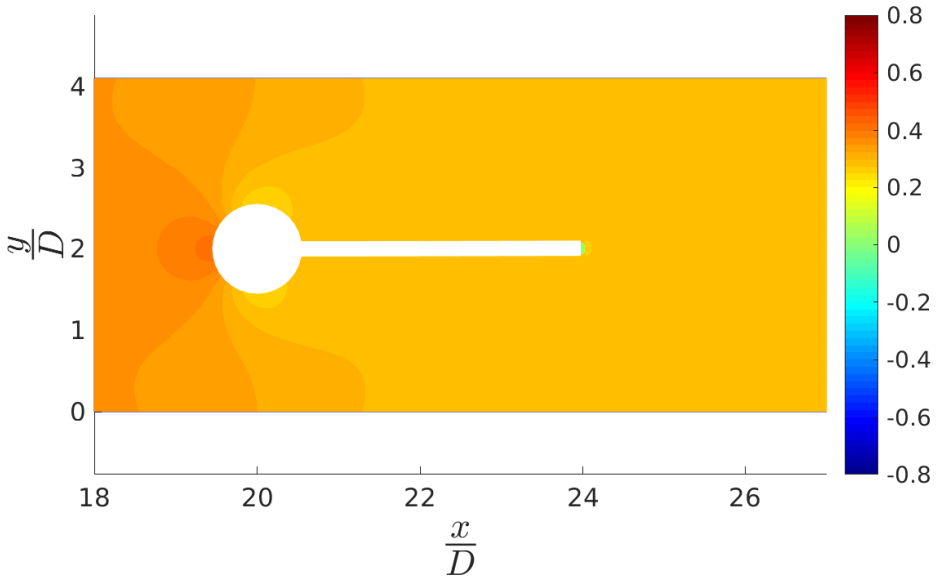

Figure 4.16: Dimensionless perturbation pressure $p' = \frac{p}{\rho_0 c_0^2}$ distribution according benchmark test FSI1 of [52] for elastic plate behind circular cylinder at Re=20, Ma=0.1.

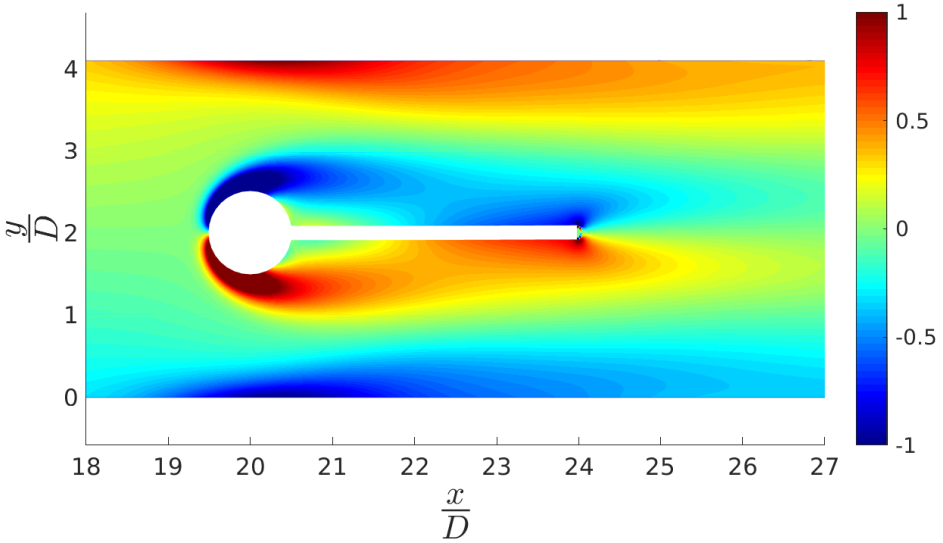

Figure 4.17: Instantaneous vorticity ω_z of the dimensionless velocity field $\vec{u}/c_0$ according benchmark test FSI1 of [52] for elastic plate behind circular cylinder at Re=20, Ma=0.1.

The results of the simulation of FSI2 is shown in Figure 4.18. This shows the periodic motion of the plate tip at point A, cf. Figure 4.1. The oscillations are comparable to those of [52] where the displacement of point A was found to be $\phi_A/D \approx 0.0123 \pm 0.802 = 1.23 \pm 80.2 \cdot 10^{-3}$[m]. From the present results the displacement for the last period of oscillation was observed to be $\phi_A/D \approx 0.0365 \pm 0.8387 = 3.65 \pm 83.87 \cdot 10^{-3}$[m]. These results are in quite good agreement and indicate that the immersed boundary method can properly describe FSI. However, instabilities that are thought to originate from the FSI-coupling made the solution unstable beyond $t = 8.76$ [s]. This is further discussed in section 4.3.1. The power added to the elastic plate system across the beam length is shown in Figure 4.23. The sinusoidal shaped power over the plate length seen at time $t = 8.25$ is the discussed instabilities. At time $t = 8.25$ the instabilities dominate the power transfer of the fluid-structure interaction. Before this time the interactions are well behaved and the growing instabilities are thought to have a negligible effect on the large-scale dynamics of the plate. From Figure 4.15 it is clear that the periodic oscillations had not reached a steady solution. The implementation of a stable solution of the FSI-coupling is needed for better results to compare with [52].

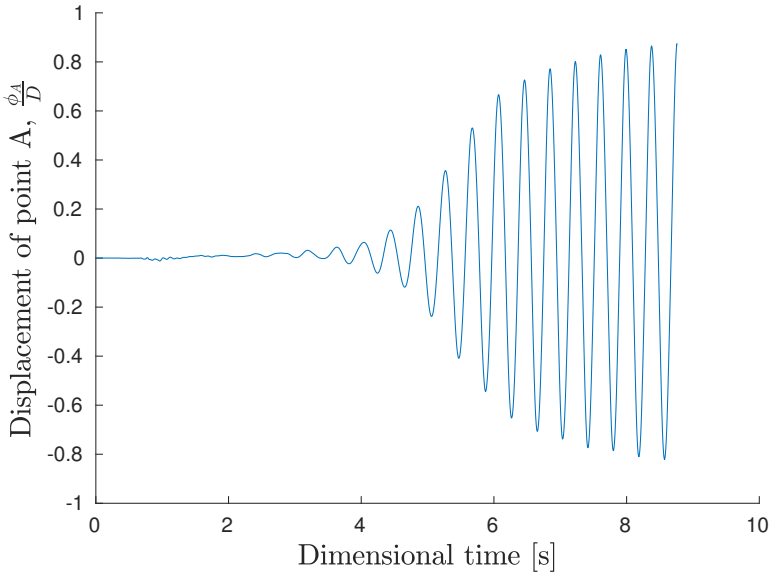

Figure 4.18: Displacement of point A $\frac{\phi_A}{D}$ over dimensional time, according benchmark test FSI2 of [52] for elastic plate behind circular cylinder, at Re=100, Ma =$\frac{1}{3}$. The dashed line indicate the time of release.

Figure 4.19 shows the dimensionless pressure near the cylinder plate arrangement for the case FSI2. The pressure varies across the plate. The pressure difference between the top and bottom side of the plate accelerates the plate upwards. Figure 4.19 shows the instantaneous vorticity of the dimensionless velocity field. As in Figure 4.20 for FSI1 a band of positive and negative vorticity is observed behind the plate. The plate motion is pushing the vorticity band to oscillate with the plate oscillations.

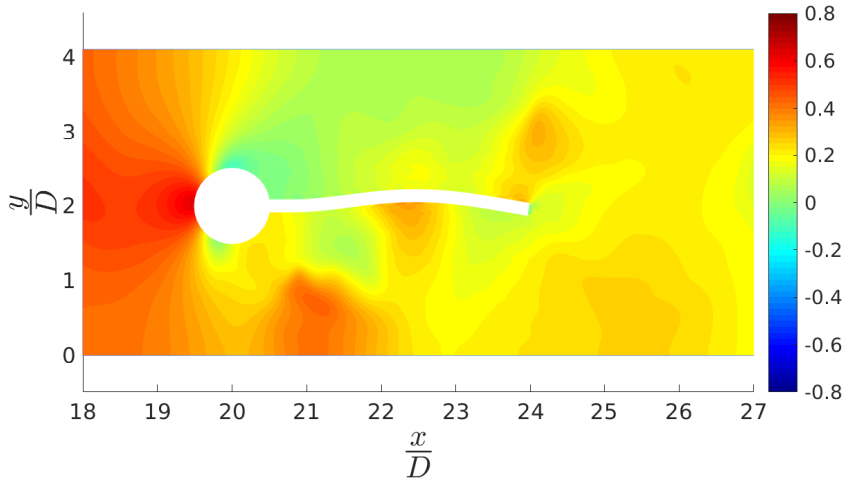

Figure 4.19: Dimensionless perturbation pressure $p' = \frac{p}{\rho_0 c_0^2}$ distribution according benchmark test FSI2 of [52] for elastic plate behind circular cylinder at Re=100, Ma=$\frac{1}{3}$.

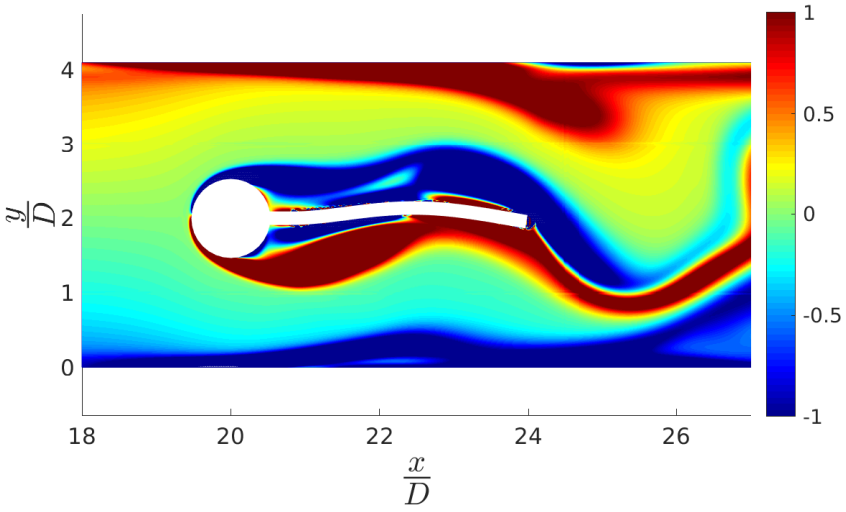

Figure 4.20: Instantaneous vorticity ω_z of the dimensionless velocity field $\vec{u}/c_0$ according benchmark test FSI2 of [52] for elastic plate behind circular cylinder at Re=100, Ma=$\frac{1}{3}$.

4.3.1 Differential pressure

A proper description of the pressure load on the plate was found to be critical for stable FSI solutions. Due to the implementation of the pressure load, certain ratios of grid point density to joint point density were prone to instabilities in the pressure load. If the joint point density and grid point density were nearly exactly matched to a whole number fraction, situations where every other joint point did not have a pressure occurred. For example with a grid size $\Delta = \frac{D}{100}$ with $m = 350$ points, corresponding to $\Delta_s = s_x^{(i+1)} - s_x^{(i)} = \frac{L}{m} \approx \frac{D}{50}$, this was an issue as this density is close to exactly half that of the grid. These situations were reduced by interpolating between nearby values. This interpolation created sporadic pressure spikes in the pressure load, thought to be caused by the ghost point configuration jumps discussed in section 3.3 b). This problem was reduced for $m = 220$ compared to $m = 350$. These pressure spikes can be seen in Figure 4.21 for the case FSI2. The spikes are suspected to cause the onset of a numerical instability of the FSI. Some small amplitude spikes were observed for the case FSI1, but these were small enough to not influence the solution at simulation end time. The pressure spikes in FSI2 should in the future be removed either by interpolation from nearby pressures or by identifying the underlying issue. The implementation of a high frequent filter to dampen the oscillatory pressure forces is also suggested. The inclusion of a non-zero damping term d in the elastic plate equations (2.18) could reduce the unstable oscillations.

4.3.2 Transfer of energy for the elastic plate

The energy exchange due to the fluid-structure interaction is investigated for the elastic plate system. The power from the fluid to the structure is as found in section 4.2.2:

$$P_f = \int_{\partial\Omega} (p n_j u_j - n_j u_i \tau_{ij}) dA \tag{4.9}$$

where $\delta\Omega$ is the boundary interface between the fluid and the structure, n_j is the unit normal vector in index notation, P_f is the work exerted from the fluid model to the structure.

The rate of change of energy in the Euler-Bernoulli equation has been evaluated by [30] and reads:

$$\frac{d}{dt}\left(\frac{1}{2}\rho_s h \int_0^L \dot{\phi}^2 dx + \frac{1}{2} B \int_0^L (\phi_{xx})^2 dx\right) = \int_0^L (-\delta p)\dot{\phi} dx - d\int_0^L \dot{\phi}^2 dx \tag{4.10}$$

The pressure load transfers energy to the system through the term $P_s = \int_0^L (-\delta p)\dot{\phi} dx$. This corresponds analytically to the fluid power term $p n_j u_j$ of eqn. (4.9). The energy from the fluid through viscous forces are however not regained in the elastic plate system. This is a consequence of the assumptions of the Euler-Bernoulli model since only loads normal to the axial dimension are considered. Since damping was set to zero for this system the exchange of energy can be investigated by looking at the pressure load power term. Figure 4.23 shows the power added to the plate across the plate length for FSI2. The most power is transferred at the plate end where the largest velocities occur. The spikes observed at $t = 5.28$ [s] and $t = 6.27$ [s] are due to spikes in the pressure load. The oscillatory

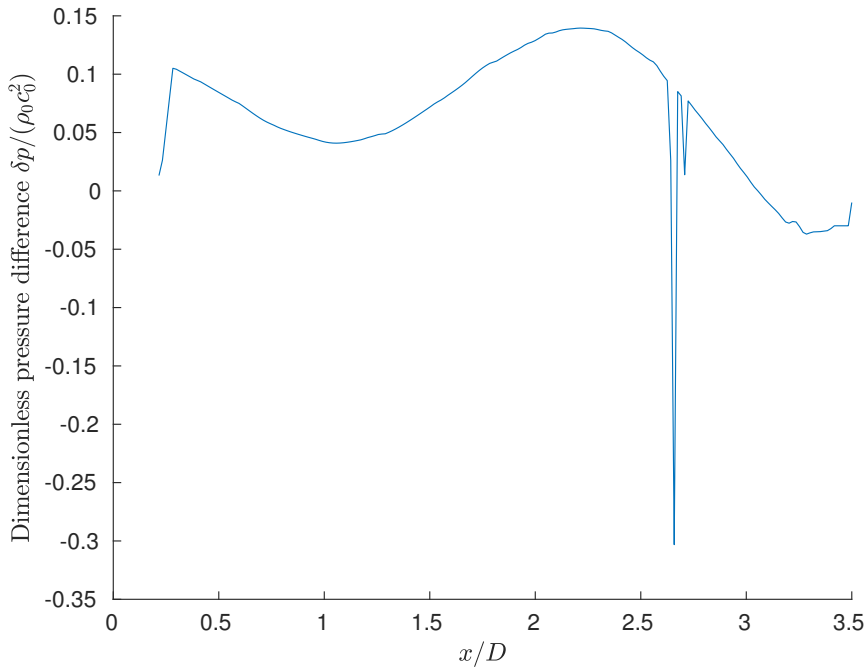

Figure 4.21: Dimensionless pressure perturbation along the joint point elements of the plate $m = 350$ for Re=100, Ma=0.1.

instabilities that are observed for FSI2 are not observed in the power transfer of FSI1, cf. Figure 4.22.

4.4 Computations

All simulations were run on the IDUN/EPIC cluster at NTNU [40]. The simulations were run on 9 nodes, one for each parallel block in the domain.
The cluster hardware specifications can be found at:
https://www.hpc.ntnu.no/pages/viewpage.action?pageId=22413575[40]
The most common computer on this cluster is included here cited from [40]:
-Dell PE630 with 2 x E5-2630 v4 10 cores 2.20GHz, 128GB RAM, 300GB local disk

Example of simulation time:
Simulation of a circular cylinder with an attached elastic plate took 90 hours for $881 \times 301 = 265181$ grid points and 106704 time steps.

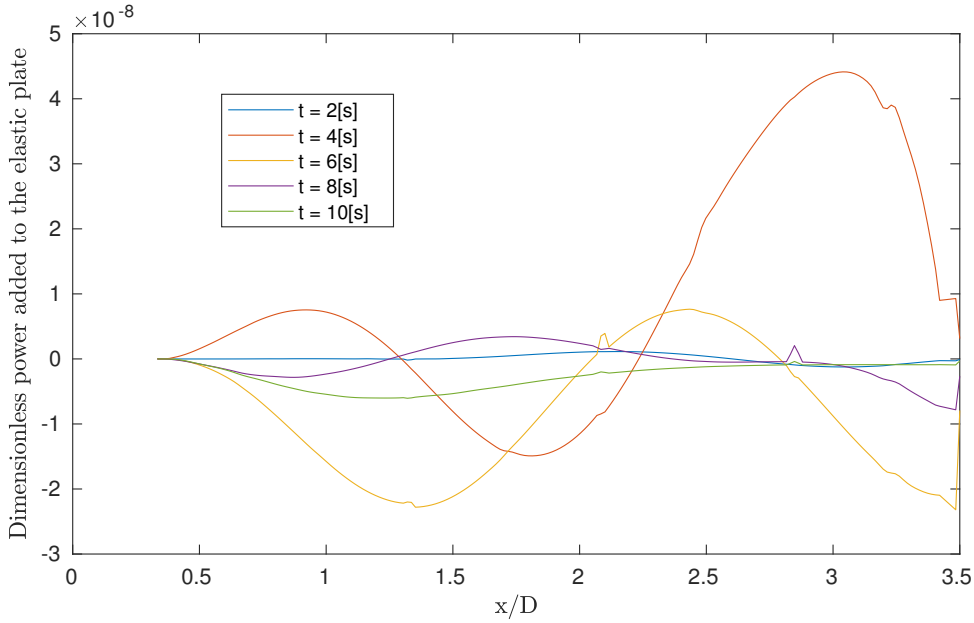

Figure 4.22: Dimensionless power $P_s = (-\delta p)\dot{\phi}$ to the plate along the dimensionless plate length with $m = 220$ for FSI1 at Re=20, Ma=0.2

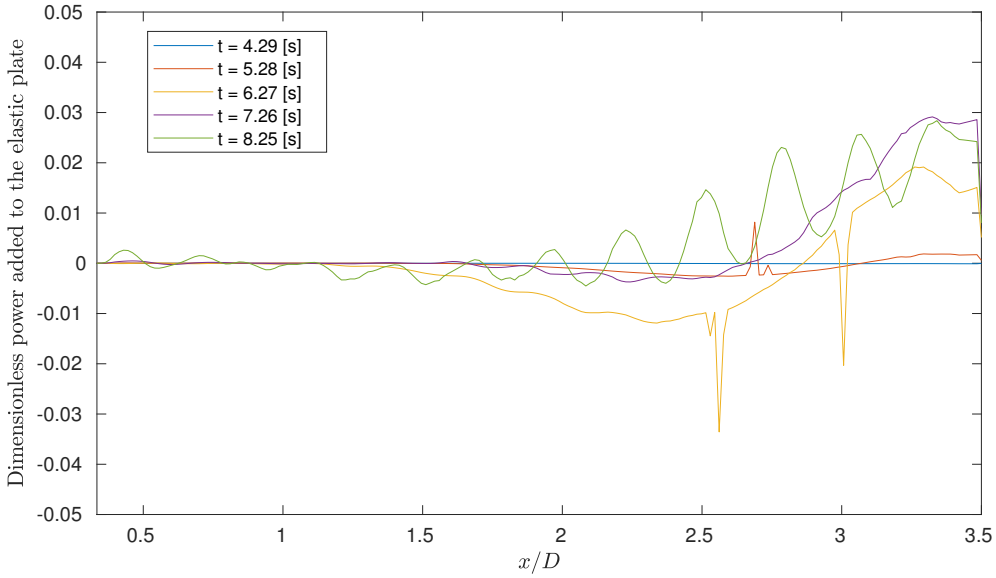

Figure 4.23: Dimensionless power $P_s = (-\delta p)\dot{\phi}$ to the plate along the dimensionless plate length with $m = 220$ for FSI2 at Re=100, Ma=1/3

Chapter 5

Conclusions

The purpose of this thesis is to investigate the higher order ghost-point immersed boundary method by Khalili [27] for fluid-structure interaction. The implementation of two FSI-cases has been presented: **a)** an elastically mounted circular cylinder in free stream and **b)** an elastic plate attached to a circular cylinder in channel flow.

a) The immersed boundary method shows quite good agreement with the results of Yang and Stern [55] and Blackburn and Karniadakis [6] for an elastically mounted circular cylinder at Re=200. Second-order ordinary differential equations governing the cylinder motion have been investigated and the order of convergence showed a dependency on the external forcing which has not been understood. The energy transfer between the fluid and the structure for an elastically mounted circular cylinder has been investigated. A pattern for the energy transfer has been presented and physical interpretations of the results have been suggested.

b) The implemented model for an elastic plate behind a circular cylinder indicates that our IBM method is able to reproduce the results of the benchmark for FSI by Turek and Hron [52]. The immersed boundary method shows the ability to impose moving and deforming geometries. However, the implementation of the pressure load on the structure is prone to interpolations errors. It is suspected that these errors are amplified by the fluid-structure interactions, which made the simulation of the test case FSI2 unstable. An issue with the higher order IBM was encountered were narrow regions did not contain the required 12 point stencil width. These regions need an estimation of the derivatives of the viscous fluxes. This problem was solved in these regions using crude assumptions. It is suggested that the derivatives of the viscous fluxes should, in the future, be calculated with a lower order SBP-operator or that an alternative local estimation of the derivatives is implemented.

Chapter 6

Future outlook

Some aspects of the current work have been left for future work due to computational- and time restrictions. The suggested points to investigate are listed below:

- The application of this IBM with FSI for other geometries and benchmarks is of interest to further verify and validate this immersed boundary method.
- The order of time convergence of the different numerical methods in section 4.2.4 is not properly understood and suspected to be caused by a programming error. The order of convergence should be further investigated for the harmonic oscillator system.
- The elastically mounted cylinder simulations should be simulated longer in time to achieve more converged steady-state solutions.
- An investigation of the temporal order of our immersed boundary method with FSI is of interest. This is a challenge to estimate as the temporal errors are dominated by the spatial errors, as discussed in [46]. The importance of solving the FSI system on synchronous intermediate time stages in the Runge-Kutta method is one aspect that would be of interest.
- Further work on the elastic plate model is needed. Insights into the growing instabilities are important for future implementation of this method with FSI. The effect of a filtering of the pressure load or inclusion of damping is suggested for the reduction of these instabilities.
- The effect of plate models for the fluid-structure interaction for the benchmark by Turek and Hron [52] should be investigated.
- The goal of the OSAS-research project is the modeling of fluid-structure interaction in the upper human airways. The implementation of the present plate model into a model of the upper human airways could give insights into the interactions between the biomechanical tissues and the airflow.

Bibliography

[1] Aasgrav, E., Johnsen, S. G., Simonsen, A. J., Müller, B., 2017. CFD Simulations of Turbulent Flow in the Human Upper Airways. SINTEF akademisk forlag.
URL http://hdl.handle.net/11250/2480176

[2] Balint, T., Lucey, A., 2005. Instability of a cantilevered flexible plate in viscous channel flow. Journal of Fluids and Structures 20 (7), 893 – 912.
URL http://www.sciencedirect.com/science/article/pii/S0889974605000757

[3] Bao, Y., Zhou, D., Tu, J., 2011. Flow interference between a stationary cylinder and an elastically mounted cylinder arranged in proximity. Journal of Fluids and Structures 27 (8), 1425–1446.

[4] Bauchau, O. A., 2009. Structural Analysis. Vol. 163 of Solid Mechanics and its Applications. Springer Netherlands.

[5] Bihs, H., Kamath, A., Alagan Chella, M., Aggarwal, A., Arntsen, Ø. A., 2016. A new level set numerical wave tank with improved density interpolation for complex wave hydrodynamics. Computers and Fluids 140, 191–208.

[6] Blackburn, H. M., Karniadakis, G. E., 1993. Two and three dimensional simulations of vortex-induced vibration of a circular cylinder. In: Third International Offshore and Polar Engineering Conference. International Society of Offshore and Polar Engineers, pp. 715–720.

[7] Bukač, M., Čanič, S., Glowinski, R., Tambača, J., Quaini, A., 2013. Fluid-structure interaction in blood flow capturing non-zero longitudinal structure displacement. Journal of Computational Physics 235, 515 – 541.
URL http://www.sciencedirect.com/science/article/pii/S0021999112004901

[8] Burton, T., Blevins, R., 1976. Vortex-shedding noise from oscillating cylinders. Journal of the Acoustical Society of America 60 (3), 599–606.

[9] Carpenter, M., Gottlieb, D., Abarbanel, S., 1994. Time-stable boundary conditions for finite-difference schemes solving hyperbolic systems: Methodology and application to high-order compact schemes. Journal of Computational Physics 111 (2), 220–236.

[10] Cheng, Y., Ji, C., Zhai, G., Oleg, G., 2017. Fully nonlinear numerical investigation on hydroelastic responses of floating elastic plate over variable depth sea-bottom. Marine Structures 55, 37 – 61.
URL http://www.sciencedirect.com/science/article/pii/S0951833916301289

[11] Cheny, Y., Botella, O., 2010. The LS-STAG method: A new immersed boundary/level-set method for the computation of incompressible viscous flows in complex moving geometries with good conservation properties. Journal of Computational Physics 229 (4), 1043–1076.

[12] Chi, C., Lee, B. J., Im, H. G., 2017. An improved ghost-cell immersed boundary method for compressible flow simulations. International Journal for Numerical Methods in Fluids 83 (2), 132–148.

[13] Doost, S. N., Ghista, D., Su, B., Zhong, L., Morsi, Y. S., 2016. Heart blood flow simulation: a perspective review. BioMedical Engineering OnLine 15 (101).

[14] Epstein, L. J., Kristo, D., Strollo, P. J., Friedman, N., Malhotra, A., Patil, S. P., Ramar, K., Rogers, R., Schwab, R. J., Weaver, E. M., Weinstein, M. D., 2009. Clinical guideline for the evaluation, management and long-term care of obstructive sleep apnea in adults. Journal of clinical sleep medicine : JCSM : official publication of the American Academy of Sleep Medicine 5 (3).

[15] Fadlun, E., Verzicco, R., Orlandi, P., Mohd-Yusof, J., 2000. Combined immersed-boundary finite-difference methods for three-dimensional complex flow simulations. Journal of Computational Physics 161 (1), 35–60.

[16] Garcia, G. C., 2016. Investigation of a fluid-structure interaction method for a flexible plate in viscous compressible channel flow. Project work. NTNU, Norwegian University of Science and Technology.
URL http://osas.no/publications

[17] Grigoriadis, D., Kassinos, S., Votyakov, E., 2009. Immersed boundary method for the mhd flows of liquid metals. Journal of Computational Physics 228 (3), 903–920.

[18] Gustafsson, B., 2008. High Order Difference Methods for Time Dependent PDE. Vol. 38 of Springer Series in Computational Mathematics. Springer Berlin Heidelberg.

[19] Haase, W., 2001. Unsteady aerodynamics including fluid/structure interaction. Air Space Europe 3 (3), 83–86.

[20] Hairer, E., Wanner, G., Lubich, C., 2006. Geometric Numerical Integration: Structure-Preserving Algorithms for Ordinary Differential Equations. Vol. 31 of Springer Series in Computational Mathematics. Springer Berlin Heidelberg.

[21] Hong, K.-S., Shah, U. H., 2018. Vortex-induced vibrations and control of marine risers: A review. Ocean Engineering 152, 300 – 315.
URL http://www.sciencedirect.com/science/article/pii/S0029801818300945

[22] Hou, G., Wang, J., Layton, A., 2012. Numerical methods for fluid-structure interaction - a review. Communications in Computational Physics 12 (2), 337–377.

[23] Hübner, B., Walhorn, E., Dinkler, D., 2004. A monolithic approach to fluidstructure interaction using space-time finite elements. Computer Methods in Applied Mechanics and Engineering 193 (23), 2087–2104.

[24] Ji, H., Lien, F.-S., Zhang, F., 2015. A gpu-accelerated adaptive mesh refinement for immersed boundary methods. Computers Fluids 118, 131 – 147.
URL http://www.sciencedirect.com/science/article/pii/S0045793015001942

[25] Kannan, R., Przekwas, A., Singh, N., Delvadia, R., Tian, G., Walenga, R., 2017. Pharmaceutical aerosols deposition patterns from a dry powder inhaler: Euler Lagrangian prediction and validation. Medical Engineering and Physics 42, 35–47.

[26] Khalili, E., Larsson, M., Müller, B., 2017. Immersed boundary method for the compressible navier-stokes equations uning high order summation by parts difference operators. Progress in Applied CFD - CFD 2017.

[27] Khalili, M., 2018. Fluid-structure interaction and immersed boundary method for the compressible Navier-Strokes equations using high order methods. Ph.D. thesis, NTNU, Norwegian University of Science and Technology, 2018:30.

[28] Khalili, M., Larsson, M., Müller, B., 2016. Interaction between a simplified soft palate and compressible viscous flow. Journal of Fluids and Structures 67, 85–105.

[29] Khalili, M. E., Larsson, M., Müller, B., 2018. Immersed boundary method for viscous compressible flows around moving bodies. Computers Fluids 170, 77 – 92.
URL https://www.sciencedirect.com/science/article/pii/S0045793018302305

[30] Khalili, M. E., Larsson, M., Müller, B., 2018. Immersed boundary method for viscous compressible flows around moving bodies. Computers Fluids 170, 77 – 92.
URL https://www.sciencedirect.com/science/article/pii/S0045793018302305

[31] Kim, S. K., Na, Y., Kim, J.-I., Chung, S.-K., 2013. Patient specific CFD models of nasal airflow: Overview of methods and challenges. Journal of Biomechanics 46 (2), 299 – 306, special Issue: Biofluid Mechanics.
URL http://www.sciencedirect.com/science/article/pii/S0021929012006744

[32] Kreiss, H.-O., Scherer, G., 1974. Finite element and finite difference methods for hyperbolic partial differential equations. Mathematical aspects of finite elements in partial differential equations, 195–212.

[33] Kreiss, H.-O., Scherer, G., 1977. On the existence of energy estimates for difference approximations for hyperbolic systems. Tech. rep., Dept. of Scientific Computing, Uppsala University.

[34] Larsson, M., 2018. Welcome to the OSAS-page. Accessed: 2018-05-25.
URL https://osas.no

[35] Larsson, M., Müller, B., 2012. Immersed boundary method for the compressible navier-stokes equations uning high order summation by parts difference operators. Progress in CFD - CFD 2012 12 (2/3), 164–175.

[36] Mattsson, K., Nordström, J., 2004. Summation by parts operators for finite difference approximations of second derivatives. Journal of Computational Physics 199 (2), 503–540.

[37] Michler, C., Hulshoff, S., van Brummelen, E., de Borst, R., 2004. A monolithic approach to fluid-structure interaction. Computers and Fluids 33 (5), 839–848.

[38] Misner, C. W., 1973. Gravitation. Freeman.

[39] Newmark, N. M., 1959. A method of computation for structural dynamics. Journal of the engineering mechanics division 85 (3), 67–94.

[40] NTNU-HPC-GROUP, 2018. NTNU HPC homepage. Accessed: 2018-06-02.
URL https://www.hpc.ntnu.no/

[41] Owlcation, C. K., 2017. Non-respiratory Functions of the Respiratory System.
URL https://usercontent2.hubstatic.com/8214455_f1024.jpg

[42] Pan, D., Shao, X., Deng, J., Yu, Z., 2014. Simulations of passive oscillation of a flexible plate in the wake of a cylinder by immersed boundary method. European Journal of Mechanics / B Fluids 46, 17–27.

[43] Peskin, C. S., 1972. Flow patterns around heart valves: A numerical method. Journal of Computational Physics 10 (2), 252–271.

[44] Poinsot, T.-J., Lele, S., 1992. Boundary conditions for direct simulations of compressible viscous flows. Journal of Computational Physics 101 (1), 104–129.

[45] Quarteroni, A., Manzoni, A., Vergara, C., 2017. The cardiovascular system: Mathematical modelling, numerical algorithms and clinical applications. Acta Numerica 26, 365–590.

[46] Ringstad, K. E., 2017. Moving immersed boundary method for compressible flow. Project work. NTNU, Norwegian University of Science and Technology.

[47] Ryzhakov, P., Rossi, R., Idelsohn, S., Oñate, E., 2010. A monolithic Lagrangian approach for fluid-structure interaction problems. Computational Mechanics 46 (6), 883–899.

[48] Schneiders, L., Günther, C., Meinke, M., Schröder, W., 2016. An efficient conservative cut-cell method for rigid bodies interacting with viscous compressible flows. Journal of Computational Physics 311 (C), 62–86.

[49] Shams, A., Lopresto, V., Porfiri, M., 2017. Modeling fluid-structure interactions during impact loading of water-backed panels. Composite Structures 171, 576 – 590.
URL http://www.sciencedirect.com/science/article/pii/S0263822316327428

[50] Strand, B., 1994. Summation by parts for finite difference approximations for d/dx. Journal of Computational Physics 110 (1), 47–67.

[51] Takács, G., Rohal-Ilkiv, B., 2012. Model Predictive Vibration Control: Efficient Constrained MPC Vibration Control for Lightly Damped Mechanical Structures. Springer London.

[52] Turek, S., Hron, J., 2007. Proposal for Numerical Benchmarking of Fluid-Structure Interaction Between an Elastic Object and Laminar Incompressible Flow. Vol. 53.

[53] Usmani, Z. A., Chai-Coetzer, C., Antic, N. A., McEvoy, R. D., 03 2013. Obstructive sleep apnoea in adults. Postgraduate medical journal 89 (1049), 148.
URL https://search.proquest.com/docview/1781650287?accountid=12870

[54] Wanderley, J. B., Souza, G. H., Sphaier, S. H., Levi, C., 2008. Vortex-induced vibration of an elastically mounted circular cylinder using an upwind tvd two-dimensional numerical scheme. Ocean Engineering 35 (14), 1533 – 1544.
URL http://www.sciencedirect.com/science/article/pii/S0029801808001261

[55] Yang, J., Stern, F., 2012. A simple and efficient direct forcing immersed boundary framework for fluid-structure interactions. Journal of Computational Physics 231 (15), 5029–5061.

[56] Zhang, L., Gerstenberger, A., Wang, X., Liu, W., 2004. Immersed finite element method. Computer Methods in Applied Mechanics and Engineering 193 (21-22), 2051–2067.